

# Super*B* Detector Technical Design Report

## Abstract

This report describes the technical design detector for Super*B*.

E. Grauges,  
**Universitat De Barcelona, Fac. Fisica. Dept. ECM Barcelona E-08028, Spain**

G. Donvito, V. Spinoso  
**INFN Bari and Università di Bari, Dipartimento di Fisica, I-70126 Bari, Italy**

M. Manghisoni, V. Re, G. Traversi  
**INFN Pavia and Università di Bergamo Dipartimento di Ingegneria Industriale, I-24129 Bergamo, Italy**

G. Eigen, D. Fehlker, L. Helleve  
**University of Bergen, Institute of Physics, N-5007 Bergen, Norway**

A. Carbone, R. Di Sipio, A. Gabrielli, D. Galli, F. Giorgi, U. Marconi, S. Perazzini, C. Sbarra,  
V. Vagnoni, S. Valentineti, M. Villa, A. Zoccoli  
**INFN Bologna and Università di Bologna, Dipartimento di Fisica, I-40127 Bologna, Italy**

C. Cheng, A. Chivukula, D. Doll, B. Echenard, D. Hitlin, P. Ongmongkolkul, F. Porter,  
A. Rakitin, M. Thomas, R. Zhu  
**California Institute of Technology, Pasadena, California 91125, USA**

G. Tatishvili  
**Carleton University, Ottawa, Ontario, Canada K1S 5B6**

R. Andreassen, C. Fabby, B. Meadows, A. Simpson, M. Sokoloff, K. Tomko  
**University of Cincinnati, Cincinnati, Ohio 45221, USA**

A. Fella  
**INFN CNAF I-40127 Bologna, Italy**

M. Andreotti, W. Baldini, R. Calabrese, V. Carassiti, G. Cibinetto, A. Cotta Ramusino,  
A. Gianoli, E. Luppi, E. Luppi, M. Munerato, L. Tomassetti  
**INFN Ferrara and Università di Ferrara, Dipartimento di Fisica, I-44100 Ferrara, Italy**

D. Stoker  
**University of California, Irvine Irvine, California 92697, USA**

O. Bezshyyko, G. Dolinska  
**Taras Shevchenko National University of Kyiv Kyiv, 01601, Ukraine**

N. Arnaud, C. Beigbeder, F. Bogard, D. Breton, L. Burmistrov, D. Charlet, J. Maalmi,  
L. Perez Perez, V. Puill, A. Stocchi, V. Tocut, S. Wallon, G. Wormser  
**Laboratoire de l'Accélérateur Linéaire, IN2P3/CNRS, Université Paris-Sud 11, F-91898 Orsay, France**

D. Brown  
**Lawrence Berkeley National Laboratory, University of California, Berkeley, California 94720, USA**

A. Calcaterra, R. de Sangro, G. Felici, G. Finocchiaro, P. Patteri, I. Peruzzi, M. Piccolo,  
M. Rama

**Laboratori Nazionali di Frascati dell'INFN, I-00044 Frascati, Italy**

S. Fantinel, G. Maron

**Laboratori Nazionali di Legnaro dell'INFN, I-35020 Legnaro, Italy**

E. Ben-Haim, G. Calderini, H. Lebbolo, G. Marchiori

**Laboratoire de Physique Nucléaire et de Hautes Energies, IN2P3/CNRS, Université  
Pierre et Marie Curie-Paris 6, F-75005 Paris, France**

R. Cenci, A. Jawahery, D.A. Roberts

**University of Maryland, College Park, Maryland 20742, USA**

D. Lindemann, P. Patel, S. Robertson, D. Swersky

**McGill University, Montréal, Québec, Canada H3A 2T8**

P. Biassoni, M. Citterio, V. Liberali, F. Palombo, A. Stabile, S. Stracka

**INFN Milano and Università di Milano, Dipartimento di Fisica, I-20133 Milano, Italy**

A. Aloisio, G. De Nardo, A. Doria, R. Giordano, A. Ordine, S. Pardi, G. Russo, C. Sciacca

**INFN Napoli and Università di Napoli Federico II, Dipartimento di Scienze Fisiche,  
I-80126, Napoli, Italy**

A.Y. Barniakov, M.Y. Barniakov, V.E. Blinov, V.P. Druzhinin, V.B. Golubev, S.A. Kononov,  
E. Kravchenko, A.P. Onuchin, S.I. Serednyakov, Y.I. Skovpen, E.P. Solodov

**Budker Institute of Nuclear Physics, Novosibirsk 630090, Russia**

M. Bellato, M. Benettoni, M. Corvo, A. Crescente, F. Dal Corso, C. Fanin, E. Feltresi,

N. Gagliardi, M. Morandin, M. Posocco, M. Rotondo, R. Stroili

**INFN Padova and Università di Padova, Dipartimento di Fisica, I-35131 Padova, Italy**

C. Andreoli, L. Gaioni, E. Pozzati, L. Ratti, V. Speziali

**INFN Pavia and Università di Pavia, Dipartimento di Elettronica, I-27100 Pavia, Italy**

D. Aisa, M. Bizzarri, C. Cecchi, S. Germani, P. Lubrano, E. Manoni, A. Papi, A. Piluso, A. Rossi

**INFN Perugia and Università di Perugia, Dipartimento di Fisica, I-06123 Perugia, Italy**

M. Lebeau

**INFN Perugia, I-06123 Perugia, Italy, and**

**California Institute of Technology, Pasadena, California 91125, USA**

C. Avanzini, G. Batignani, S. Bettarini, F. Bosi, M. Ceccanti, A. Cervelli, A. Ciampa,  
F. Crescioli, M. Dell'Orso, D. Fabiani, F. Forti, P. Giannetti, M. Giorgi, S. Gregucci, A. Lusiani,  
P. Mammini, G. Marchiori, M. Massa, E. Mazzoni, F. Morsani, N. Neri, E. Paoloni, E. Paoloni,  
M. Piendibene, A. Profeti, G. Rizzo, L. Sartori, J. Walsh, E. Yurtsev

**INFN Pisa, Università di Pisa, Dipartimento di Fisica, and Scuola Normale Superiore,  
I-56127 Pisa, Italy**

D.M. Asner, J. E. Fast, R.T. Kouzes,  
**Pacific Northwest National Laboratory, Richland, Washington 99352, USA**

A. Bevan, F. Gannaway, J. Mistry, C. Walker  
**Queen Mary, University of London, London E1 4NS, United Kingdom**

C.A.J. Brew, R.E. Coath, J.P. Crooks, R.M. Harper, A. Lintern, A. Nichols, M. Staniztki,  
R. Turchetta, F.F. Wilson  
**Rutherford Appleton Laboratory, Chilton, Didcot, Oxon, OX11 0QX, United Kingdom**

V. Bocci, G. Chiodi, R. Faccini, C. Gargiulo, D. Pinci, L. Recchia, D. Ruggieri  
**INFN Roma and Università di Roma La Sapienza, Dipartimento di Fisica, I-00185 Roma, Italy**

A. Di Simone  
**INFN Roma Tor Vergata and Università di Roma Tor Vergata, Dipartimento di Fisica, I-00133 Roma, Italy**

P. Branchini, A. Passeri, F. Ruggieri, E. Spiriti  
**INFN Roma Tre and Università di Roma Tre, Dipartimento di Fisica, I-00154 Roma, Italy**

D. Aston, M. Convery, G. Dubois-Felsmann, W. Dunwoodie, M. Kelsey, P. Kim, M. Kocian,  
D. Leith, S. Luitz, D. MacFarlane, B. Ratcliff, M. Sullivan, J. Va'vra, W. Wisniewski, W. Yang  
**SLAC National Accelerator Laboratory Stanford, California 94309, USA**

K. Shougaev, A. Soffer  
**School of Physics and Astronomy, Tel Aviv University Tel Aviv 69978, Israel**

F. Bianchi, D. Gamba, G. Giraud, P. Mereu  
**INFN Torino and Università di Torino, Dipartimento di Fisica Sperimentale, I-10125 Torino, Italy**

G. Dalla Betta, G. Fontana, G. Soncini  
**INFN Padova and Università di Trento, ICT Department, I-38050 Trento, Italy**

M. Bomben, L. Bosisio, P. Cristaudo, G. Giacomini, D. Jugovaz, L. Lanceri, I. Rashevskaya,  
G. Venier, L. Vitale  
**INFN Trieste and Università di Trieste, Dipartimento di Fisica, I-34127 Trieste, Italy**

R. Henderson  
**TRIUMF Vancouver, British Columbia, Canada V6T 2A3**

J.-F. Caron, C. Hearty, P. Lu, R. So  
**University of British Columbia, Vancouver, British Columbia, Canada V6T 1Z1**

P. Taras  
**Université de Montréal, Physique des Particules, Montréal, Québec, Canada H3C 3J7**

A. Agarwal, J. Franta, J.M. Roney  
**University of Victoria, Victoria, British Columbia, Canada V8W 3P6**



# Contents

<b>1</b>	<b>Particle Identification</b>	<b>1</b>
1.1	Summary of Physics Requirements and Detector Performance goals 3-4 pages . . .	1
1.1.1	Physics requirements Cincinnati, Maryland . . . . .	1
1.1.2	Detector concept . . . . .	1
1.1.3	Charged Particle Identification . . . . .	2
1.2	Particle Identification Overview 2-3 pages . . . . .	2
1.2.1	Experience of BaBar DIRC . . . . .	2
1.2.2	Barrel PID: Focusing DIRC (FDIRC) . . . . .	3
1.3	Projected Performance of FDIRC 2-3 pages . . . . .	6
1.3.1	Reconstruction Arnaud, Roberts . . . . .	6
1.3.2	MC Simulation . . . . .	6
1.3.3	Effect of Background on performance Roberts, Arnaud, Cenci, Vavra, Kravchenko . . . . .	7
1.4	The Barrel FDIRC Detector Overview 5-10 pages . . . . .	7
1.4.1	Impact on other systems Benettoni, Simi, Vavra . . . . .	7
1.4.2	Photodetectors . . . . .	7
1.4.3	Laser calibration system . . . . .	15
1.4.4	FDIRC Mechanical Design 5 pages . . . . .	16
1.4.5	Mechanical support . . . . .	16
1.4.6	Electronics readout, High and Low voltage . . . . .	24
1.4.7	Integration issues 2 pages . . . . .	28
1.4.8	DAQ and computing 1 page . . . . .	30
1.4.9	FDIRC R&D Results until now 2-3 pages . . . . .	30
1.4.10	Ongoing FDIRC R&D 1-2 pages . . . . .	32
1.4.11	System Responsibilities and Management 1-2 pages . . . . .	32
1.4.12	Cost, Schedule and Funding Profile 1-2 pages . . . . .	32

# 1 Particle Identification

Chapter editors: Nicolas Arnaud & Jerry Va'vra

The current version of the plan for the TDR PID chapter can be found at [http://mailman.fe.infn.it/superbwiki/images/8/8c/PID\\_TDR\\_plan.pdf](http://mailman.fe.infn.it/superbwiki/images/8/8c/PID_TDR_plan.pdf)

## 1.1 Summary of Physics Requirements and Detector Performance goals 3-4 pages

---

### 1.1.1 Physics requirements Cincinnati, Maryland

#### 1.1.2 Detector concept

The DIRC (Detector of Internally Reflected Cherenkov light) [1] is an example of innovative detector technology that has been crucial to the performance of the *BABAR* science program. DIRC main performance parameters are the following: (a) a measured time resolution per photon of  $\sim 1.7\text{ns}$ , close to the PMT transit time spread of  $1.5\text{ns}$ , (b) a single photon Cherenkov angle resolution of  $9.6\text{mrad}$  for tracks from di-muon events, (c) a Cherenkov angle resolution per track of  $2.5\text{mrad}$  in di-muon events, and (d)  $\pi K$  separation greater than  $2.5\sigma'$  over the entire track momentum range from the pion Cherenkov threshold up to  $4.2\text{GeV}/c$ .

An excellent DIRC S/N performance did not come without some effort, and this experience is useful for knowing how we want to design FDIRC at SuperB. To obtain the final background performance it was necessary to: (a) apply a tight timing cut of  $\pm 8\text{ns}$  around each event, (b) add a substantial shielding around

the beam pipe under DIRC, which reduced the PMT background by at least a factor of 6x, (c) install many background detectors (here we found, for example, that a rate in neutron detectors correlates with the DIRC background very well, indicating a common origin), and (d) improve operation of the machine. After  $\sim 10$  years of operation the PMT gain was reduced by  $\sim 30\%$ . The electronics dead time was limited to  $\sim 5\%$  at a rate of  $\sim 250\text{kHz}/\text{PMT}$ .

Excellent flavor tagging will continue to be essential for the program of physics anticipated at SuperB, and the gold standard of particle identification in this energy region is that provided by internally reflecting ring-imaging devices (the DIRC class of ring imaging detectors). The challenge for SuperB is to retain (or even improve) the outstanding performance attained by the *BABAR* DIRC [2], while also gaining an essential factor of 100 in background rejection to deal with the much higher luminosity.

A new Cherenkov ring imaging detector is being planned for the SuperB barrel, called the Focusing DIRC, or FDIRC. It will use the existing *BABAR* bar boxes and mechanical support structure. This structure will be attached to a new photon "camera", which will be optically coupled to the bar box window. The new camera design combines a small modular focusing structure that images the photons onto a focal plane instrumented with very fast, highly pixelated, photon detectors (PMTs) [4]. These elements should combine to attain the desired performance levels while being at least 100 times less sensitive to backgrounds than the *BABAR* DIRC, while achieving the same PID performance as BaBar DIRC.

To cope with higher luminosity, FDIRC's photon camera will provide the overall safety factor of  $250\times$  compared to *BABAR* DIRC, because it will be:

- 25× smaller than DIRC water-based camera;
- its new highly pixilated photon detectors will be about 10× faster;
- the photon camera is built using radiation resistant Fused silica material, instead of water or oil, which is more sensitive to the neutron background.

Furthermore, (a) the entire system will have  $\sim 18\text{k}$  pixels, (b) will reconstruct photons in 3D ( $x$ ,  $y$ , and time), (c) the Cherenkov angle can be reconstructed based on pixels alone, however, time is included in the final PID likelihood hypothesis, (d) time also plays the important role in FDIRC to reduce the background, and (e) the expected timing resolution of  $\sigma \sim 200\text{ps}$  will also make it possible to reduce the chromatic broadening of Cherenkov angle resolution by  $0.5\text{-}1\text{mrad}$ , depending on photon propagation path length.

Several options were under consideration for a possible PID detector in the forward direction: (a) “DIRC-like TOF” time-of-flight (TOF) [5], (b) pixelated TOF [6] and (c) Aerogel RICH [7]. The chosen technology, based on time-of-flight technique, has been selected by the SuperB collaboration in May 2011 and room has been reserved in the SuperB design to accommodate this new detector on the forward side. Tests of a full-scale prototype of one sector of the “Forward Time-Of-Flight” (FTOF) detector are foreseen in near future; if they are successful, the FTOF will be included in the SuperB baseline.

### 1.1.3 Charged Particle Identification

The charged particle identification at SuperB relies on the same framework as the BABAR experiment. Electrons and muons are identified by the EMC and the IFR respectively, aided by  $dE/dx$  measurements in the inner trackers (SVT and DCH). Separation for low-momentum hadrons is primarily provided by  $dE/dx$ . At higher momenta (above  $0.7\text{ GeV}/c$  for pions and kaons, above  $1.3\text{ GeV}/c$  for protons), a dedicated

system, the FDIRC – inspired by the successful BABAR DIRC – will perform the  $\pi/K$  separation.

## 1.2 Particle Identification Overview 2-3 pages

---

### 1.2.1 Experience of BaBar DIRC

The BABAR DIRC – see Fig. 1.1 – is a novel ring-imaging Cherenkov detector. The Cherenkov light angular information, produced in ultra-pure synthetic fused silica bars, is preserved while propagating along the bar via internal reflections to the camera (the SOB) where an image is produced and detected.

The entire DIRC has 144 quartz bars, each  $4.9\text{ m}$  long, which are set along the beam line and cover the whole azimuthal range. Thanks to an internal reflection coefficient of  $\sim 0.9997$  and orthogonal bar faces, Cherenkov photons are transported to the back end of the bars with the magnitude of their angles conserved and only a modest loss of photons. They exit into a pinhole camera consisting of a large volume of purified water (a medium chosen because it is inexpensive, transparent, and easy to clean, with average index of refraction and relative chromatic dispersion sufficiently close to those of the fused silica). The photon detector PMTs are located at the rear of the SOB, about  $1.2\text{ m}$  away from the quartz bar exit window.

The reconstruction of the Cherenkov angle uses information from the tracking system together with the positions of the PMT hits in the DIRC. In addition, information on the time of arrival of hits is used in rejecting background hits, and resolving ambiguities.

The BABAR DIRC performed reliably and efficiently over the whole BABAR data taking period (1999-2007). Its physics performance remained consistent throughout the run period, although some upgrades, such as the addition of shielding and replacement of electronics, were necessary to cope with machine conditions. Its main performance parameters are the following:



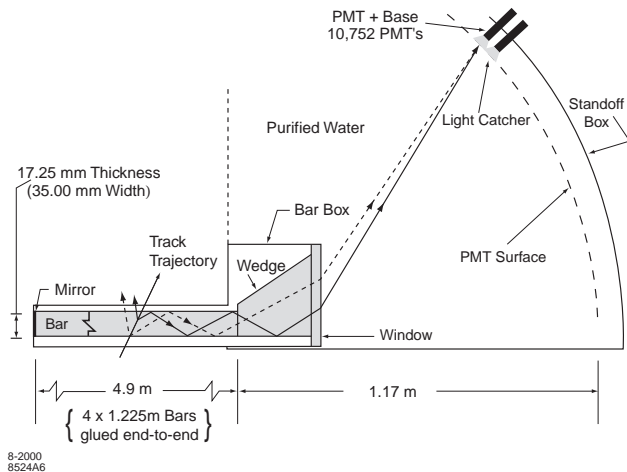


Figure 1.1: Schematic of the *BABAR* DIRC.

- measured time resolution of about 1.7 ns, close to the PMT transit time spread of 1.5 ns;
- single photon Cherenkov angle resolution of 9.6 mrad for dimuon events;
- Cherenkov angle resolution per track of 2.5 mrad in dimuon events;
- $K - \pi$  separation above 2.5 ' $\sigma$ ' from the pion Cherenkov threshold up to 4.2 GeV/c.

### 1.2.2 Barrel PID: Focusing DIRC (FDIRC)

As discussed above, the PID system in Super*B* must cope with much higher luminosity-related background rates than in *BABAR* – current estimates are on the order of 100 times higher. The basic strategy is to make the camera much smaller and faster. A new photon camera imaging concept, based on focusing optics, is therefore envisioned. The focusing blocks (FBLOCK), responsible for imaging the Cherenkov photons onto the PMT cathode surfaces, would be machined from radiation-hard pieces of fused silica. The major design constraints for the new camera are the following: (a) it must be consistent with the existing *BABAR* bar box design, as these elements will be reused in Super*B*; (b) it must coexist with the *BABAR* mechanical support and magnetic field

constraints; (c) it requires very fine photon detector pixelation and fast photon detectors.

Imaging is provided by a mirror structure focusing onto an image plane containing highly pixelated photomultiplier tubes. The reduced volume of the new camera and the use of fused silica for coupling to the bar boxes (in place of water as it was in *BABAR* SOB), is expected to reduce the sensitivity to background by about one order of magnitude compared to *BABAR* DIRC. The very fast timing of the new PMTs is expected to provide many additional advantages: (a) an improvement of the Cherenkov resolution; (b) a measure of the chromatic dispersion term in the radiator [8, 9, 11]; (c) separation of ambiguous solutions in the folded optical system; and (d), another order of magnitude improvement in background rejection.

Figure 1.2 shows the new FDIRC camera design (see Ref. [4, 12] for more detail). It consists of two parts: (a) a focusing block (FBLOCK) with cylindrical and flat mirror surfaces, and (b) a new wedge. The wedge at the end of the bar rotates rays with large transverse angles (in the focusing plane) before they emerge into the focusing structure. The old wedge is too short so that an additional wedge element must be added to insure that all rays strike the cylindrical mirror. The cylindrical mirror is rotated appropriately to make sure that all rays reflect onto the FBLOCK flat mirror, preventing reflections back into the bar box itself; the flat mirror then reflects rays onto the detector focal plane with an incidence angle of almost  $90^\circ$ , thus avoiding reflections. The focal plane is located in a slightly under-focused position to reduce the FBLOCK size and therefore its weight. Precise focusing is unnecessary, as the finite pixel size would not take advantage of it. The total weight of the solid fused silica FBLOCK is about 80 kg. This significant weight requires good mechanical support.

There are several important advantages gained in moving from the *BABAR* pinhole focused design with water coupling to a focused optical design made of solid fused silica: (a) the design is modular; (b) sensitivity to background, especially to neutrons, is significantly

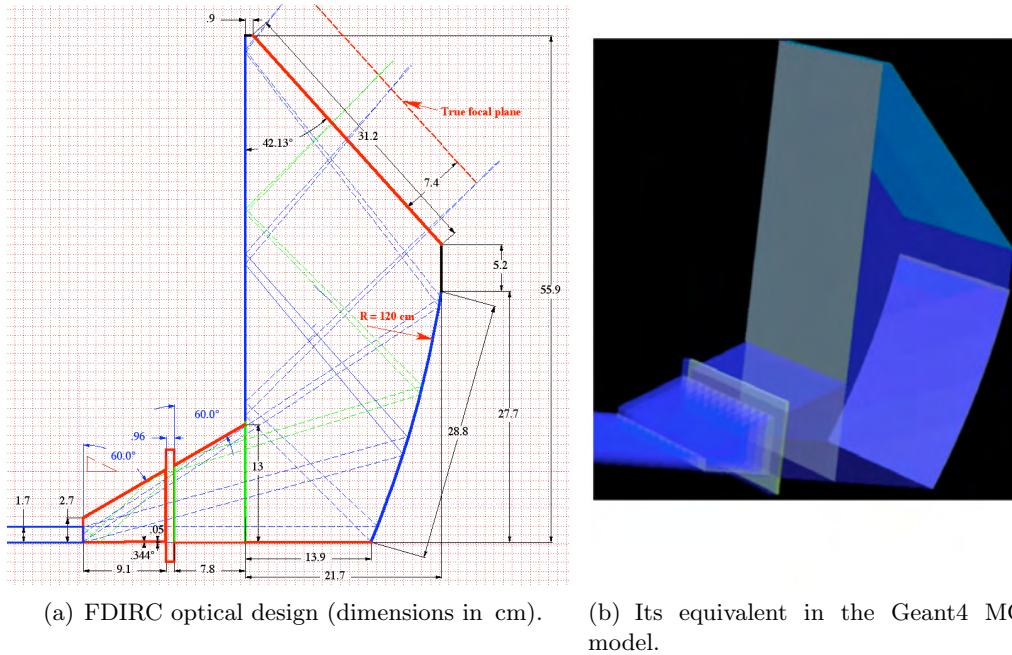


Figure 1.2: Barrel FDIRC Design.

reduced; (c) the pinhole-size component of the angular resolution in the focusing plane can be removed by focusing with cylindrical mirror, and timing can be used to measure the chromatic dispersion, thus improving performance; (d) the total number of photomultipliers is reduced by about one half compared to a non-focusing design with equivalent performance; (e) there is no risk of water leaks into the SuperB detector, and no time-consuming maintenance of a water system, as was required to operate *BABAR* safely.

Each new camera will be attached to its *BABAR* bar box with an optical RTV glue, which will be injected in a liquid form between the bar box window and the new camera and cure in place. As Fig. 1.2 shows, the cylindrical mirror focuses in the radial ( $y$ ) direction, while pinhole focusing is used in the direction out of the plane of the schematic (the  $x$ -direction). Photons that enter the FBLOCK at large  $x$ -angles reflect from the parallel sides, leading to an additional ambiguity. However, the folded design makes the optical piece small, and places the photon detectors in an accessible location, improving both the mechanics and the background sensitivity.

Since the optical mapping is 1 to 1 in the  $y$ -direction, this “folding” reflection does not create an additional ambiguity. Since a given photon bounces inside the FBLOCK only 2-4 times, the requirements on surface quality and polishing for the optical pieces are much less stringent than that required for the DIRC bar box radiator bars.

As an intermediate step towards an upgrade of DIRC for the SuperB detector, we have built and tested the 1st FDIRC prototype, in order to learn how to design a smaller FDIRC with new highly pixilated fast detectors [8, 11]. This prototype demonstrated for the first time that the chromatic correction could be done with timing. The principle is displayed in Fig. 1.3: Analytical correlation between the change of the Cherenkov angle and the change in time-of-propagation (TOP), relative to the mean wavelength of 410nm. Figure 1.4 shows the same graph with the real data for photons propagating 10 meters in the bar. Figure 1.5 shows a final result of the chromatic correction in the beam test data. One can see that the chromatic correction improves the Cherenkov angle

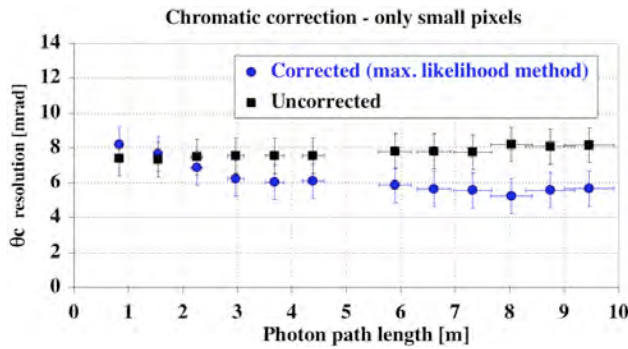


Figure 1.5: Beam test data showing the effect of the chromatic correction for  $3\text{mm} \times 12\text{mm}$  pixels obtained with H-9500 MaPMT in the 1-st FDIRC prototype. Note that the SuperB active region starts 1-2 meters from the detector camera end. Results with the H-8500 MaPMT are similar, but with slightly worse resolution [8, 11].

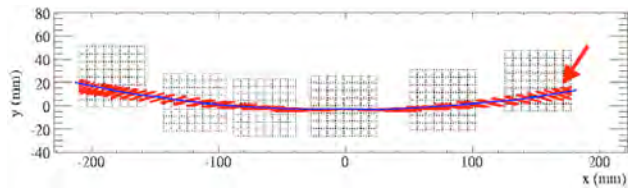


Figure 1.6: Optical ring aberration near the ring wings for the 1-st FDIRC prototype with overlaid detectors and their pixels to show that it is a substantial effect. Calculated for a position in the middle of a bar [8].

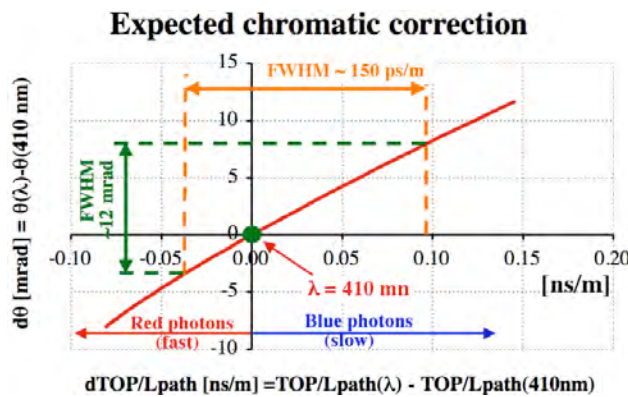


Figure 1.3: Analytical correlation between the change of the Cherenkov angle and the change in TOP, relative to the mean wavelength of 410nm [8, 11].

### Correlation in data, 10m photon path

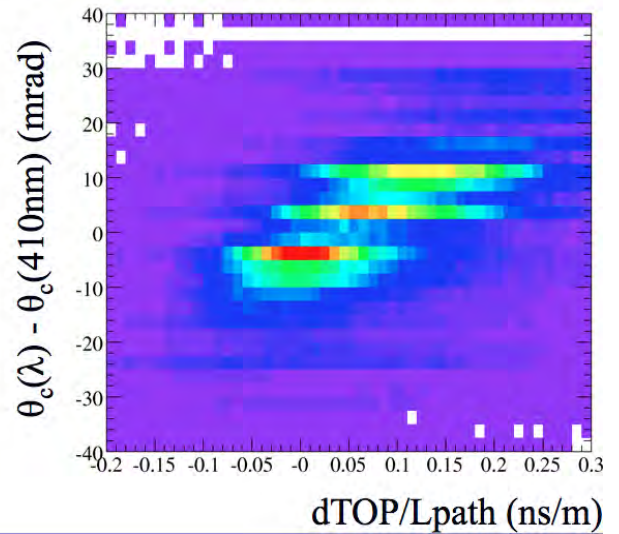


Figure 1.4: The same correlation between the change of the Cherenkov angle and the change in TOP for photons propagating 10 meters in the bar, as seen in the beam test data in the 1-st FDIRC prototype [8, 11].

resolution by 0.5-1mrad depending on photon propagation path length. To achieve this, a single photoelectron timing resolution of  $\sim 200\text{ps}$  is required. This can be achieved with H-8500 or H-9500 MaPMTs.

We have also learned from the 1st prototype that the Cherenkov ring has worse resolution on its wings than its center due to the optical aberration caused by the bar, which is amplified by a mirror. Figures 1.6 and 1.7 show that this error contribution goes from 0 mrad (at ring center) to  $\sim 9$  mrad (near the ring's wings) and it is z-dependent. This aberration is present in the non-focusing BaBar DIRC as well, but it is smaller, i.e., the mirror amplifies this effect. The effect is similar for spherical, parabolic and spherical mirrors. For more details see Ref. [12].

Each DIRC wedge inside an existing bar box has a 6 mrad angle at the bottom. This was



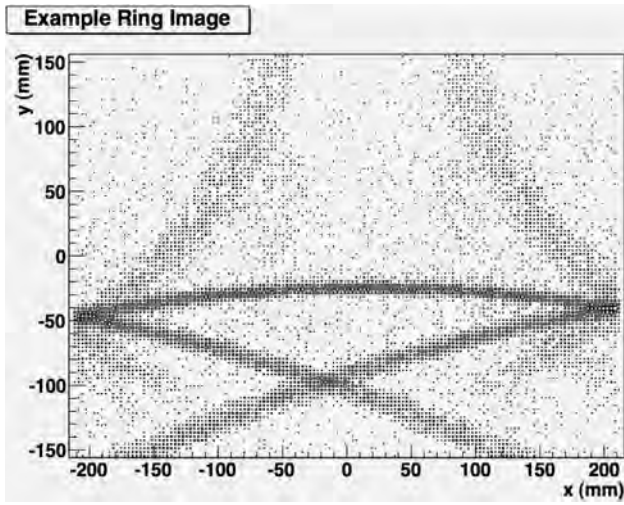


Figure 1.8: Cherenkov ring image from GEANT4 for tracks with  $\theta_{dip} = 90^\circ$  in the central bar at 4 GeV/c [13].

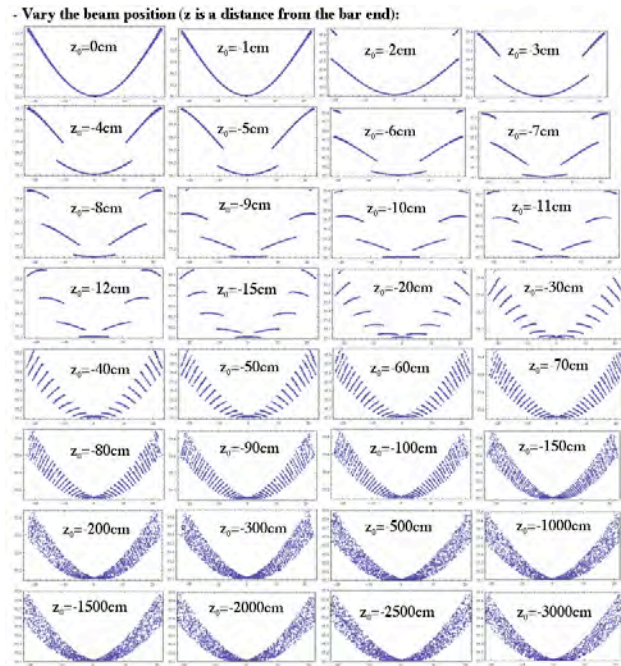


Figure 1.7: Optical ring aberration near the ring wings for the 1-st FDIRC prototype as a function of  $z$ -position along the bar [12].

done intentionally in *BABAR* to provide simple step-wise “focusing” of rays leaving the bar towards negative  $y$  to reduce the effect of bar thickness. However, in the new optical system, having this angle on the inner wedge somewhat worsens the design FDIRC optics resolution. There are two choices: (a) either leave it as it is, or (b) glue a micro-wedge at the bottom of the old wedge, inside the bar box, to correct for this angle. Though (b) is possible in principle, it is far from trivial, as the bar box must be opened. Because of this difficulty we have decided for the option (a).

Figure 1.8 shows a Cherenkov ring image for one of the central bars in the new FDIRC. It is more complicated than those from BaBar DIRC or the 1-st FDIRC prototype. This is due to reflections from the sides of the FBLOCK, and it is different for each bar. The image is actually three dimensional and can be simplified if one uses TOP as a way to slice it. The ring radius is not used in the analysis. Instead, we use a dictionary of MC assignments for each pixel:  $k_{pixel}$  ( $k_x, k_y, k_z$ ), and time-of-propagation for direct and indirect photons  $TOP_{direct}$  and  $TOP_{indirect}$  for tracks with  $\theta_{dip} = 90^\circ$  and  $z = z_{middle}$  for each bar. For any other track direction one can then calculate the Cherenkov angle simply as a dot product of two vectors:  $\cos \theta_C = k_{track} \cdot k_{pixel}$ . This procedure has been used successfully with the 1-st FDIRC prototype in the cosmic ray telescope with 3D tracking.

### 1.3 Projected Performance of FDIRC 2-3 pages

#### 1.3.1 Reconstruction Arnaud, Roberts

#### 1.3.2 MC Simulation

Fast simulation Arnaud

Full simulation Roberts

FDIRC Design	Option	$\theta_C$ resolution [mrad]
1	3 mm $\times$ 12 mm pixels with a micro-wedge	8.1
2	3 mm $\times$ 12 mm pixels and no micro-wedge	8.8
3	6 mm $\times$ 12 mm pixels with a micro-wedge	9.0
4	6 mm $\times$ 12 mm pixels and no micro-wedge	9.6

Table 1.1: FDIRC performance simulation by Geant4 MC [13].

### 1.3.3 Effect of Background on performance [Roberts, Arnaud, Cenci, Vavra, Kravchenko](#)

## 1.4 The Barrel FDIRC Detector Overview [5-10 pages](#)

---

### 1.4.1 Impact on other systems [Benettoni, Simi, Vavra](#)

### 1.4.2 Photodetectors

**Photon Detector choice** There were two photon detectors under consideration, the H-8500 (64 pixels) and the H-9500 (256 pixels) multi-anode PMTs (MaPMT) by Hamamatsu. We prefer the 12-dynode H-8500 tube from several reasons: it is the tube preferred by the medical community and therefore produced in a larger quantity, it has much smaller price than the H-9500 MaPMT, it has a smaller single electron timing spread ( $\sigma_{TTS} \sim 140$  ps vs.  $\sigma_{TTS} \sim 220$  ps), it can be obtained with somewhat enhanced QE ( $\sim 24\%$  vs.  $\sim 20\%$ ), it has more

uniform gain response across its face (1:2 vs. 1:5), and Hamamatsu strongly recommends this tube to keep a reasonable delivery schedule of large quantities. On the other hand, the H-9500 MaPMT can provide finer sampling in the y-direction and thus provides significantly better Cherenkov angle resolution. At present we have selected the H-8500 detector.

The performance of the new FDIRC is simulated with a Geant4 based program [13]. Preliminary results for the expected Cherenkov angle resolution are shown in Table 1.1 for different layouts [4]. Design #1, which has emerged as the preferred one (a 3 mm  $\times$  12 mm pixel size with the micro-wedge glued in) gives a resolution of  $\sigma \sim 8.1$  mrad per photon for 4 GeV/c pions at 90° dip angle. The micro-wedge option was supposed to remove a  $\sim 6$  mrad inclined surface on the old wedge, but this was judged as too difficult to implement in practice and was discarded. The present preferred option is #4, which would give  $\sigma \sim 9.6$  mrad per photon. This would be a performance about the same as in BaBar DIRC [2]. However, if the chromatic correction would be implemented successfully, one could reduce the error by 0.5-1 mrad depending on photon path length [11].

During the prototyping stage we used H-8500C tube with HV cable having SHV connector for convenience. However, in the final application we would use H-8500D tube, which has a special connector (SAMTEC SQT-102-01-L-S) for the HV and ground entry distributed from the motherboard. The tube has an internal HV divider, so one has to distribute only one voltage. In the following we will consider only H-8500 tube and we mean a D-version. This tube comes with a 1.5 mm-thick Borosilicate glass window with a spectral sensitivity between 300 and 650 nm. We would require a minimum QE of  $\sim 24\%$ , which corresponds to a blue sensitivity index of 9.5. The dark anode current of this tube is very low (0.1 nA per pixel and 6 nA total), and the after-pulse rate is also almost negligible. Given a design of the dynode structure preventing the direct ion backflow to the photocathode, we expect a nominal cathode

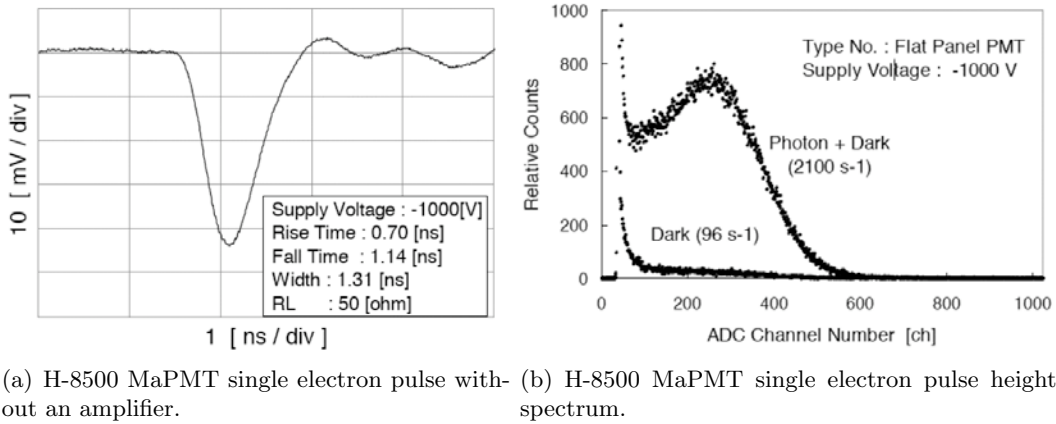


Figure 1.9: H-8500 MaPMT single electron pulse, noise and single electron pulse height distribution (Hamamatsu data).

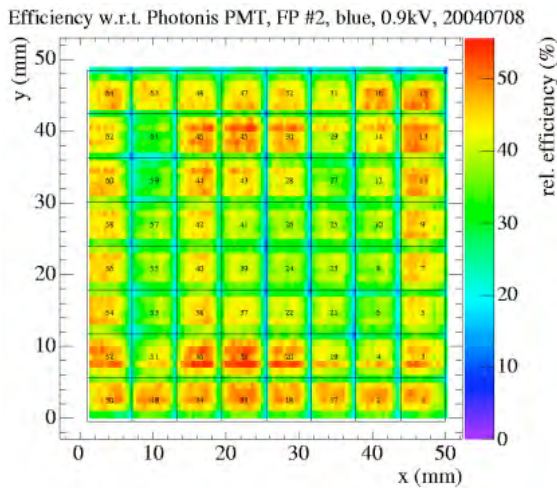


Figure 1.10: Single photoelectron response of H-8500 with  $6\text{mm} \times 6\text{mm}$  pixels [14].

PMT aging behavior, although we do not have any data at present.

Figures 1.9 show (a) a single photoelectron pulse from H-8500 before the amplification at  $\sim 1.0\text{ kV}$ , (b) a single electron pulse height spectrum. As one can see from the Hamamatsu info of Fig. 1.9, the rise time of H-8500 tube is about 0.7 ns. With SLAC amplifier, based on the Analog devices chip AD8000, the amplified rise time was about 1.5 ns, which is sufficient for our purpose. We believe that the tube needs

an amplifier with an effective gain of  $\sim 40\times$  if one is using a LeCroy 4413 discriminator with a threshold of  $\sim 25\text{ mV}$ . Hamamatsu also tells us that the pulse height spectra are not uniform across all pixels in H-8500 tube. How this effect translates into the detection efficiency depends on a type of electronics, noise level and threshold; it will be studied in detail in the FDIRC prototype first using the SLAC amplifier with the IRS-2 waveform digitizing electronics [18], and then be compared to the SuperB CFD electronics [16] - see section 8.4.6.

Figure 1.10 shows the single photoelectron efficiency of H-8500 tube, normalized to Photonis Quantacon XP2262/B PMT [14]. This plot was measured with the Elantek amplifier with a gain of  $\sim 40$  and discriminator threshold of  $-25\text{ mV}$ , and PiLas laser with 407 nm wavelength. We plan to short two neighboring pixels in the x-direction, as there is only pin-hole focusing available, and thus create either  $3\text{ mm} \times 12\text{ mm}$  pixels (H-8500), providing 32 readout channels per tube. Each photon camera would have 48 H-8500 MaPMT detectors, which corresponds to a total of 576 tubes for the entire SuperB FDIRC, resulting in 18432 pixels in the entire system. The H-8500 tube has a pixel size  $5.8\text{ mm} \times 5.8\text{ mm}$ , with a pitch between pixels equal to 6.08 mm, the effective detection area of



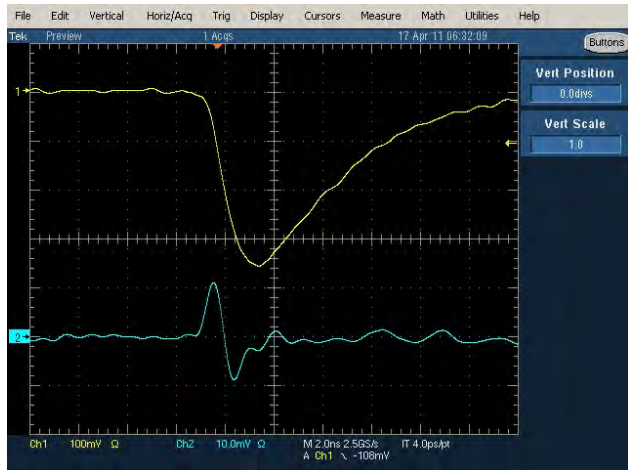


Figure 1.12: The H-8500 tube pixel-to-pixel cross talk was measured to be  $\sim 3\%$  [19].

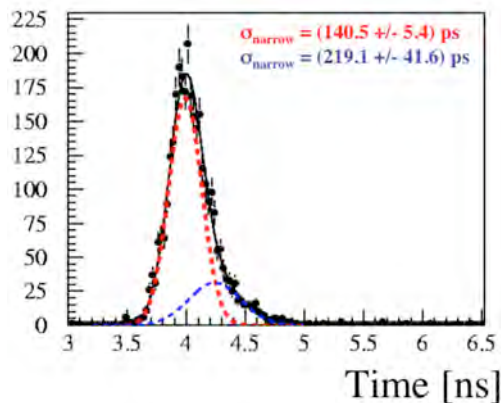


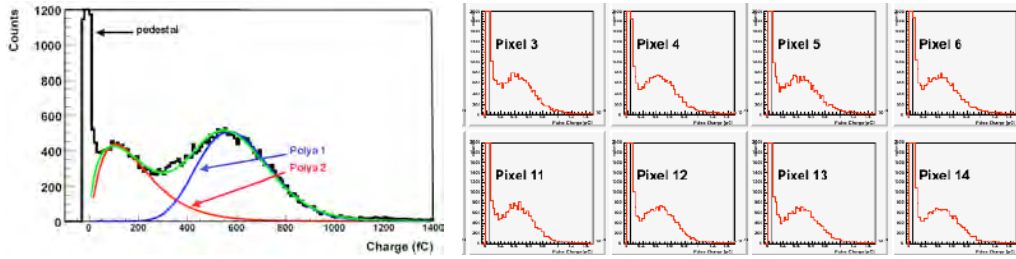
Figure 1.11: Single photoelectron transit time resolution of H-8500, obtained in a laser test, is  $\sigma_{TTS} \sim 140\text{ps}$  [14].

49 mm  $\times$  49 mm, and the H-8500 tube s total area of 52 mm  $\times$  52 mm.

Figure 1.11 shows its timing resolution to single photoelectrons ( $\sigma_{TTS} \sim 140\text{ps}$  for H-8500 [14]). This timing performance, coupled to the electronics timing resolution contribution of  $\sigma_{Electronics} \sim 100\text{ps}$ , allows corrections of the chromatic error for photon path length of more than 2 m [11], as long as the total timing resolution per single photon is  $\sigma \sim 200\text{ps}$ . The pulse rise time is  $\sim 0.8\text{ns}$ .

There are two effects to take into account when considering interaction between two neighboring pixels: a pixel-to-pixel cross-talk, and the charge sharing of the avalanche charge between two pixels. The neighbor pixel-to-pixel cross talk was measured [19] to be  $\sim 3\%$  (see Fig. 1.12). We hoped to utilize the charge sharing, which is related to the avalanche size, to reduce the size of pixels in the y-direction by charge interpolation. However, the attempt to utilize the charge sharing was not successful in this particular tube as it has entrance focusing electrodes defining pixel boundaries, which sweep electrons away from pixel boundaries, *i.e.* Hamamatsu has designed the MaPMT electrode structure in such a way to suppress the charge sharing in these tubes. Both H-8500 and H-9500 have this charge sharing-suppressing feature. Such feature does not exist in MCP-PMT detectors.

Another special feature of all MaPMT detectors is a double Polya distribution, one corresponding to a photoelectron produced at the cathode and the amplification utilizing all 12 dynodes (this is a nominal distribution), and another one corresponding to a case that a photon produces a photoelectron striking the very first dynode rather than at the photocathode, and the amplification is utilizing only 11 dynodes instead of 12. Missing one amplification stage produces a gain 2-3 smaller than the nominal amplification process, pulses arrive 2-2.5 ns earlier and (see Fig. 1.14) [19]). Figure 1.15 shows a time spectrum of normal photoelectrons produced at the cathode, pre-pulse spectrum produced at the 1-st dynode arriving  $\sim 2.5\text{ns}$  earlier, and backscattered photoelectrons arriving  $\sim 6\text{ns}$  later [26]. Figures 1.13 show resulting single electron pulse height spectra either a small shoulder near the pedestal at lower gain [20], or a clear double-Polya distribution at higher gain [21]. Although the pre-pulses are a nuisance, they can be used as normal photoelectrons in the Cherenkov ring analysis and their time can be calibrated out. Their time shift will not affect the chromatic correction, which has a range of only  $\sim 1\text{ns}$ .



(a) Double-Polya fit to single electron distribution as observed in R7600-03-M16 MaPMT. The lower peak originates from photoelectrons which are missing one amplification stage in the MaPMT [21]. (b) Single electron distributions in H-8500 MaPMT. The lower peak shows up only as a shoulder [20].

Figure 1.13: Single electron pulse height distribution in MaPMTs.

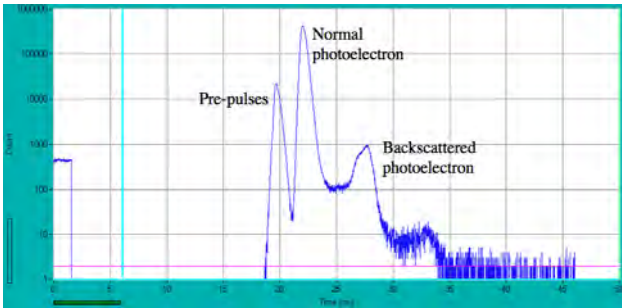


Figure 1.15: The H-8500 single electron time spectrum showing normal photoelectrons, pre-pulses and the backscattered photoelectrons [26].

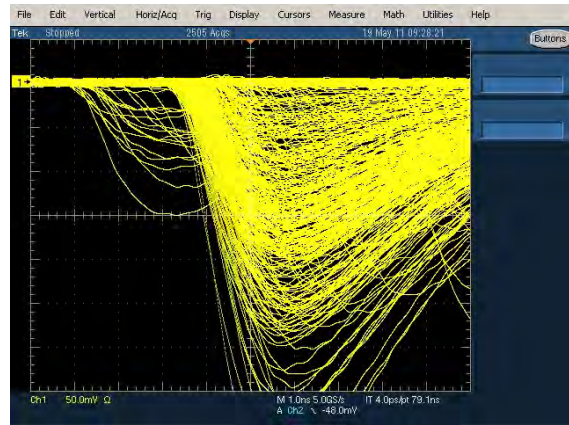


Figure 1.14: The H-8500 single electron pre-pulses corresponding to a case when a photon produces a photoelectron at the very first dynode rather than at the photocathode, and the amplification is utilizing only 11 dynodes instead of 12 [19].

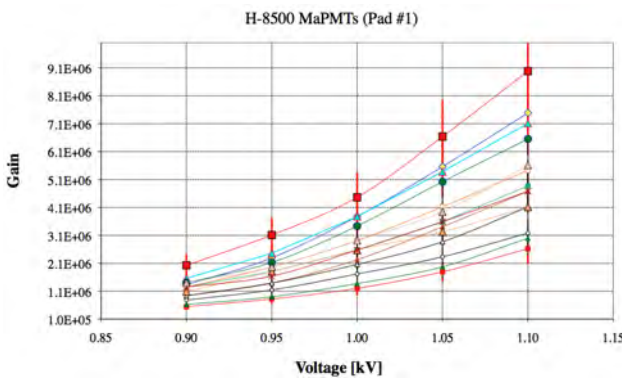
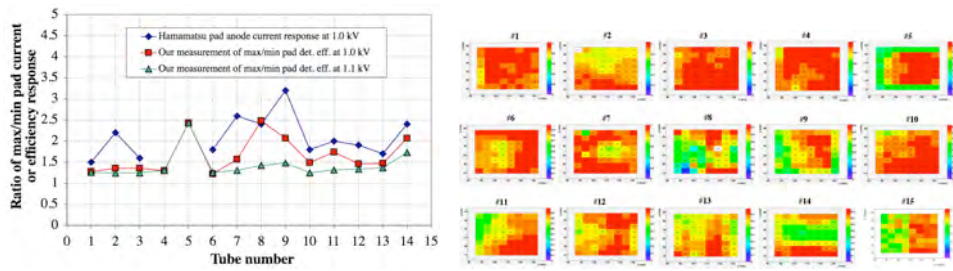


Figure 1.16: The H-8500 tube gain range and dependence on voltage for 14 tubes using pixel 1 in each tube [19].

Figure 1.16 shows that the H-8500 tube gain range is  $1 - 3 \times 10^6$  for nominal operating voltage of  $-1.0\text{ kV}$  [19]. There is a variation of gain from pixel-to-pixel due to non-uniformities in the multi-anode structure. As a result there is a variation in detection efficiency.

Figure 1.17 shows scans of 15 tubes [19], operating at  $-1.0\text{ kV}$  and  $-1.1\text{ kV}$ , amplifier gain of  $\sim 40\times$ , a threshold electronics of  $-25\text{ mV}$ , and indicates that typically the best-to-worst single electron detection efficiency might vary as much





(a) Min-max efficiency uniformity of 64 pixels. This is compared to anode current response across 64 pixels to a fixed photon flux. (b) Relative efficiency scan of 15 H-8500 tubes operating at -1.0 kV, normalized to XP2262/B min-max response across 64 pixels to PMT).

Figure 1.17: 2D single electron detection efficiency across pixels of 15 H-8500 tubes [19].

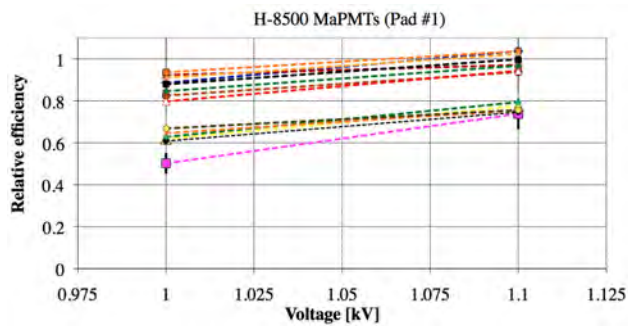


Figure 1.18: The H-8500 single electron detection efficiency dependence on voltage [19].

as 1:2 across the H-8500 PMT face. This is compared to the anode current response across all pixels to a fixed high photon flux (Hamamatsu data). Figure also shows the efficiency scans of 15 tubes [19], all operating at 1.0kV, with an amplifier gain of 40×, with a simple threshold electronics, and normalized to the Photonis Quantacon XP2262/B PMT. It indicates that the best-to-worst detection efficiency variation is as much as 1:2 across the H-8500 PMT face. Notice that the detection efficiency relative to the Quantacon XP2262/B PMT is typically at a level of 40-50% for the worst pixels, and 80-100% for the best pixels.

Figure 1.18 shows how the H-8500 tube single electron detection efficiency dependency on voltage [19]. One can see that one can improve

the detection efficiency by 10-20% per 100V increase.

There are three possible ways to deal with the pixel-based gain non-uniformity: (a) process each tube, equipped with the final electronics, in the scanning setup and simply record the individual relative efficiency values and simply feed them into analysis data base, or (b) adjust a discriminator threshold on each pixel, or (c) adjust an amplifier gain on each pixel. This concept has yet to be worked out in detail as this effect depends on details of final electronics. One should remember, when doing the overall gain adjustment, that the absolute maximum voltage on H-8500 is -1.1 kV. We want to stay below about -1.05 kV for the initial setting to have enough headroom for later period when the detector will loose gain due to aging.

**Modularity: photodetector mechanical packing fraction** There are two factors to consider when determining the photon coverage: (a) detection coverage in the focal plane of the photon camera, and (b) coverage within each tube (we will consider detection losses within the dynode structure later and loss factors later). Figure 1.19 shows the H-8500 matrix of 48 tubes in one photon camera. The size of each H-8500 tube is  $52.0 \pm 0.3$  mm, and a gap between each tube is  $\sim 0.5$  mm; this gives a contribution to the packing fraction of  $\sim 98.6\%$ . The photon packing density (effective area/external size) within each tube is  $\sim 89\%$ . These factors give the overall photon packing efficiency

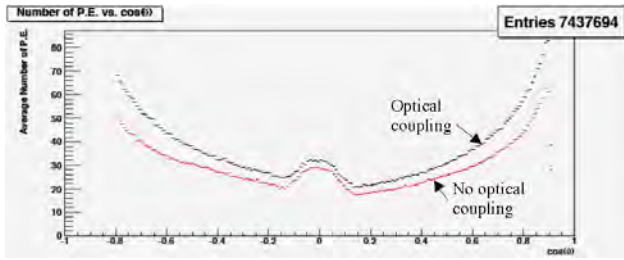


Figure 1.20: Simulated (Geant4 MC) number of photoelectrons as a function of the polar angle for two cases: with and without the optical coupling between detector face and the FBLOCK [13].

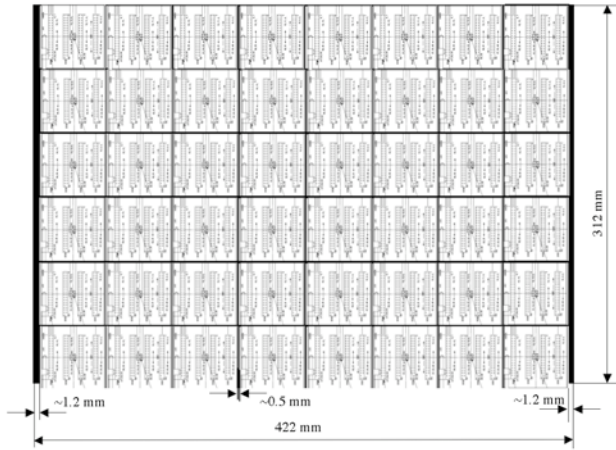


Figure 1.19: Detector matrix on one FDIRC detector camera with 48 H-8500 MaPMTs. The entire FDIRC system needs 576 tubes and 18,432 pixels [4].

of  $\sim 88\%$  for the photon camera based on 48 H-8500 tubes.

**Photon detector mechanical support** Photon detectors will be supported by the electronics motherboard. The original scheme to have one large motherboard for all 48 detectors was considered as too difficult to implement in practice. Instead we will smaller motherboards supporting groups of 6 detectors running in vertical direction. (yet to be written)

### Optical coupling of detectors to FBLOCK

The MC simulation shows (see Fig. 1.20) that we loose 8-25% of photons if we do not optically couple PMTs to the FBLOCK [13]. The event Cherenkov angle resolution ( $\sigma \sim 2.94$  mrad) improves by  $\sim 10\%$  with the optical coupling [13]. On the other hand, an access to a single failed detector will become complicated, and we may have to abandon a concept of one large single motherboard. If we use the optical coupling, we are considering eight vertical segments, each handling 6 detectors; each segment could be removable by sliding it vertically off the FBLOCK. In addition, we have not yet selected the optical coupling grease. One should realize that any leak of the grease on the FBLOCK's side optical surfaces, would result in a serious loss of photoelectrons. The optical coupling concept has yet to be tested to investigate its practicality, reliability and radiation hardness, and therefore it remains an open issue.

### Temperature requirements in Fbox enclosure

There are two major sources of heat in the detector enclosure: (a) HV resistor dividers, and (b) electronics. Each tube has a HV divider. All dividers together draw  $\sim 9$ W per 48 tubes, which is a trivial amount of heat. Assuming for now that the electronics will dissipate  $\sim 10$ W per package, one gets a total amount of heat of  $\sim 500$ W per 48 detectors. We will need a water cooled heat exchanger.

Another worry is what happens if we loose cooling. Based on our tests with FDIRC prototype detector enclosure we think that the temperature will rapidly climb beyond  $\sim 80^{\circ}\text{C}$ . That would be dangerous for tubes, optical grease coupling, glues and also could create mechanical stresses. Therefore we need an automatic power shutoff system.

### Rates and aging issues in H-8500 PMTs

One strong point of our design is that we share a total photon background load from a single bar box among 48 H-8500 detectors, and this results in acceptable rate even at the highest luminosity, and an acceptable total charge load after 10 years of operation.

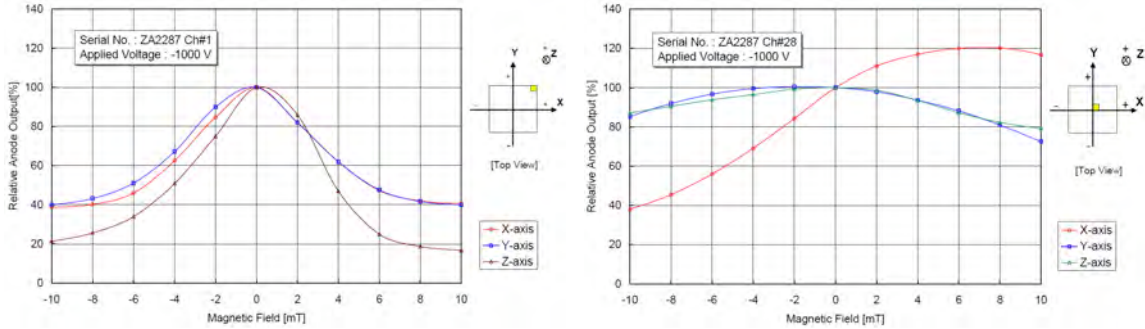
We use two methods to estimate FDIRC rates: (a) empirical scaling from Belle-I Aerogel counter rates and assuming that it scales as the luminosity (we use Belle-I rates rather than BaBar rates because that machine is believed to be closer to the SuperB for the background scaling). (b) We then use the MC simulation, which simulates all physics background processes involved in the background production and includes the precise modeling of beam line magnet components all the way up to 16 meters from IP in either direction, and uses correct FDIRC geometry with a proper handling of optical photons. The MC simulation shows that the rate is dominated by the radiative Bhabha scattering (thus our assumption above that it scales as the luminosity is justified). The empirical scaling (ES) method is rather close to the MC prediction (MC) for the contribution from a section within the active detector volume: 75 kHz (ES) vs. 85 kHz (MC) per double-pixel, or 2.4 MHz (ES) vs. 2.7 MHz (MC) per tube, which would correspond to the total accumulated charge of  $0.8\text{C}/\text{cm}^2$ (ES) vs.  $1.1\text{C}/\text{cm}^2$ (MC) for a total integrated luminosity of  $L_{int} \sim 50\text{ab}^{-1}$ . However, the contribution from the photon camera, which is outside of the magnet, is much higher without a shielding: 120 kHz (ES) vs. 550 kHz (MC) per double-pixel. This means that we need a background shield similar to what was necessary for *BABAR* DIRC. The dominating background is due to the BaBha scattering, the Touschek effect's contribution is less than 10%.

Given a design of the H-8500 dynode structure, which prevents the direct ion backflow to the photocathode, we expect the MaPMT tube cathode-aging rate to be similar to a usual PMT aging behavior, which means that the above numbers appear to be safe. For example, BaBar DIRC PMTs accumulated at least  $\sim 150\text{C}$  per tube during  $\sim 10$  years of BaBar operation and tubes have lost some efficiency ( $\sim 30\%$ ), but operated well until the end with a few voltage adjustments to correct the gain loss. This tells us that our nominal starting voltage should not exceed  $\sim 1.05\text{kV}$  to allow possible later gain ad-

justments. One should, however point out that aging tests were yet to be done for the H-8500 tube. One should also worry about unusual background conditions caused by the machine misbehavior, changes in tune, beam losses, etc., especially in the early periods before reaching the full luminosity. Hamamatsu recommends that the absolute maximum current is  $\sim 100\mu\text{A}$  per tube or  $\sim 2\mu\text{A}$  per pixel. Another constraint is a capability of the electronics to cope with high rates. SuperB FDIRC electronics can handle rates up to  $\sim 20\text{MHz}$  per pixel, if one pixel is firing, and up to  $\sim 2.5\text{MHz}$  per tube if all pixels are firing. (We still need to add a total number of neutrons per  $\text{cm}^2$  per year, rate of slow protons from np collisions, rate of ions, and expected dose obtained by electronics. All this after the background shielding and magnetic shielding are added correctly).

**Magnetic shield of H-8500 PMTs** For BaBar DIRC PMTs, which have a classical PMT dynode design, it was necessary to keep the magnetic field below  $\sim 1$  Gauss to prevent a serious degradation of pulse height spectra [2]. To do that it was necessary to enclose the entire photon camera into a large magnetic shield. Figure 1.21 shows the effect of the magnetic field on the H-8500 tube pulse height. One can notice that the effect is different near tube's boundary compared to its central region. We conclude that we can tolerate a residual magnetic field up to a level of a few Gauss with no effect on the pulse height. We plan to use a magnetic shield similar to that of *BABAR*.

**Prediction of number of photoelectrons per ring** Figure 1.22 shows FDIRC's wavelength bandwidth [4]. One can see that we operate in the visible wavelength region and that the effective filter is the Epotek 301-2 epoxy. Assuming a peak QE of 24%, and no optical grease coupling between PMTs and the FBLOCK, one obtains  $\sim 32$  photoelectrons for tracks with  $\theta_{dip} = 90^\circ$  using a simple spreadsheet calculation. Figure 1.23 shows the MC simulation of number of photoelectrons as a function of the dip angle [13]. At  $\theta_{dip} = 90^\circ$  it predicts  $\sim 27$  photoelectrons. We find the FDIRC performance



(a) The effect on boundary pixels.

(b) The effect on pixels near center.

Figure 1.21: Magnetic field effect on the H-8500 MaPMT’s pulse height (Hamamatsu data).

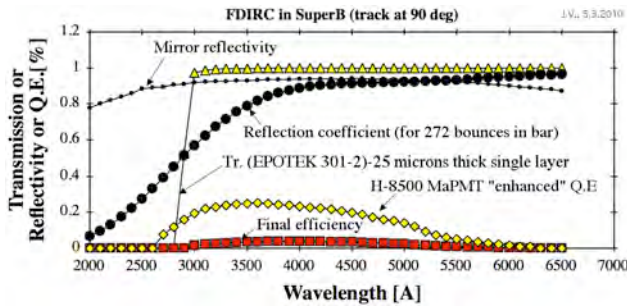


Figure 1.22: FDIRC wavelength response is limited on low wavelength side by EPOTEK 301-2 glue used to glue bars together [4].

slightly better than the DIRC performance in BABAR [2]. (numbers are still being checked)

**Radiation damage of optical components**

We used the Co<sup>60</sup> source for the irradiation of the glue samples. First, we have investigated the radiation damage of Corning 7980 Fused Silica 3mm-thick coupons used for support of glue samples and, as expected, found no loss of transmission up to 250krads. Figure 1.24 shows the irradiation of the Epotek 301-2 epoxy, used for coupling of the New Wedge to the bar box window, and the Shin-Etsu 403 RTV, used for coupling of the FBLOCK and the New Wedge. We show that these glues are acceptable for the SuperB conditions, although the Epotek 301-2 does see some small loss of transmission [23].

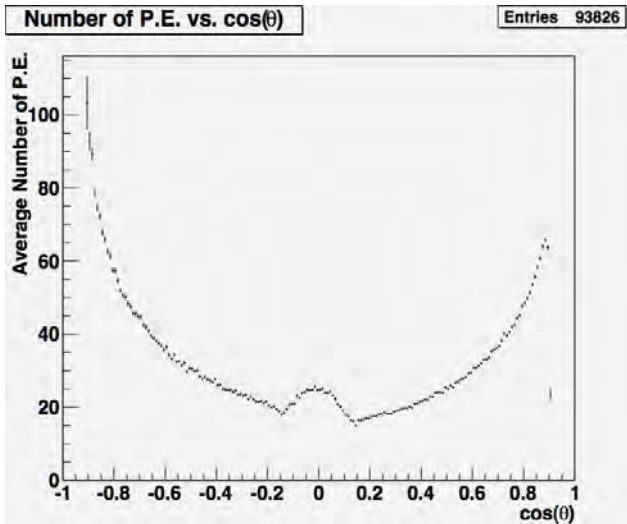


Figure 1.23: MC simulation of number of photoelectrons in FDIRC [13].



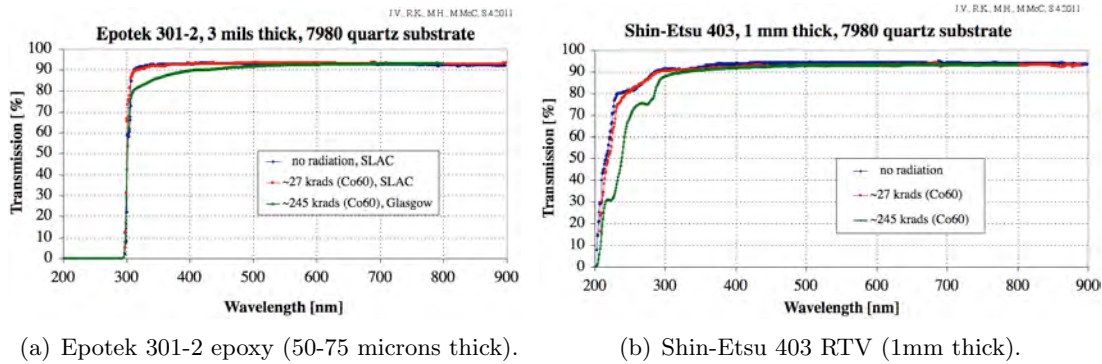


Figure 1.24: Radiation damage by the  $\text{Co}^{60}$  source of glues used in the construction of the photon camera [23].

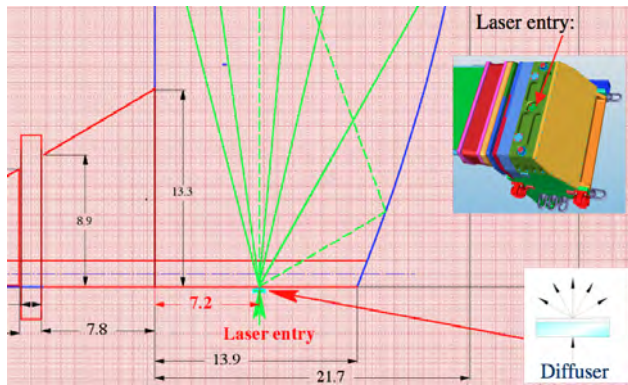


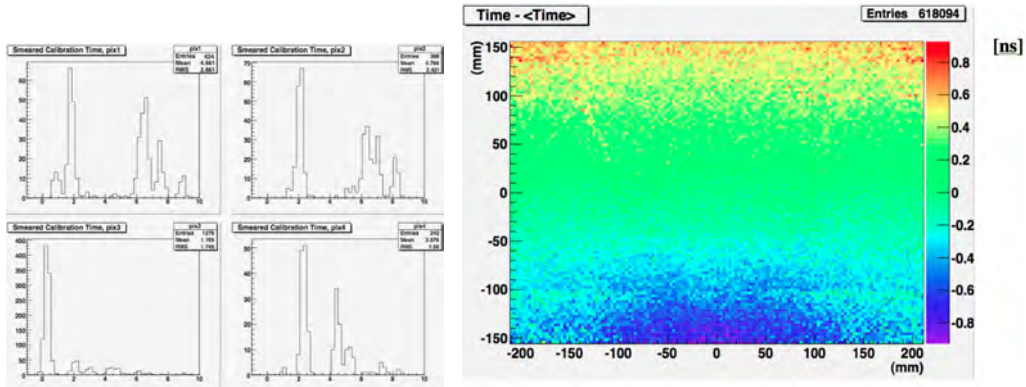
Figure 1.25: Laser entry into the FBLOCK [19].

### 1.4.3 Laser calibration system

**Optics of calibration** The aim of this calibration is twofold: (a) check the operation of tubes and electronics, (b) provide pixel offset constants for FDIRC timing calibration, which was found to be useful in the 1-st FDIRC prototype doing the chromatic corrections [19]. Figure 1.25 shows the laser entry into the FBLOCK as implemented in the final FDIRC prototype. The fiber plugs into a connector with a lens (F230FC-A), which makes a parallel laser beam, which then strikes a 5mm diameter Opal diffuser, which was selected out of several choices for its uniform light diffusing effect. The small

diameter diffuser is necessary to limit losses of real Cherenkov photons. We found experimentally that the best arrangement is if the diffuser is pressing against the bottom surface of the FBLOCK with a help of the spring (no gluing as it affects a uniformity of the scattered light). There is one fiber entry per one photon camera serving one bar box. Figure 1.26 shows MC simulation indicating that a total time spread across the focal plane is about 2 ns, which will have to be corrected out to get a single  $t_0$ . It also shows an example of the MC simulation of time of arrival in a single pixel. It shows multiple peaks corresponding to direct light and various FBLOCK side reflections. We believe that we will be able to determine timing offsets with enough precision using selected significant peaks. This calibration scheme is going to be tested in the final FDIRC prototype.

**Laser and fiber optics choice** We will use the Pilas laser diode providing a light with 407nm. We would like to split the light from one Pilas source into 6 branches, but the fiber splitter has yet to be tested to check that splitting is equal. If this works we will need two Pilas control units serving the entire system. The Pilas control unit can be triggered externally so we can control both the timing and when the calibration should happen.



(a) Time peaks from the laser calibration as it appears in several pixels [13]. (b) Laser time spread is a few ns across the focal plane [13].

Figure 1.26: Laser calibration timing.

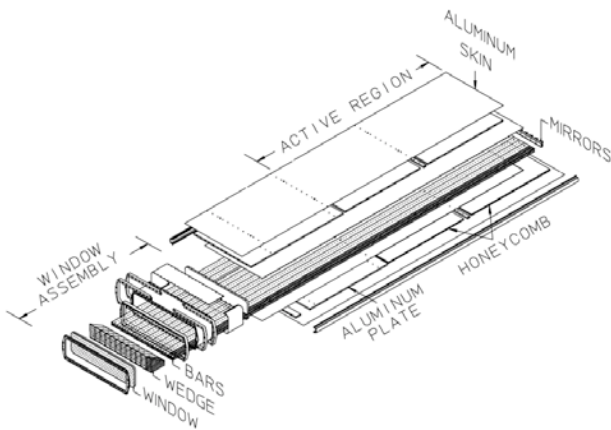


Figure 1.27: BaBar DIRC bar box [2].

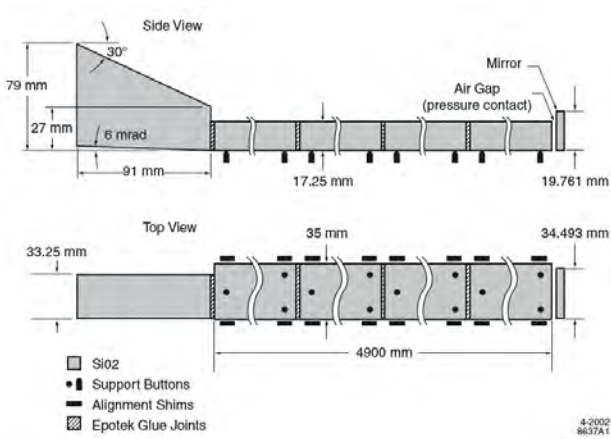


Figure 1.28: One bar segment with nominal dimensions [2].

1.4.4 FDIRC Mechanical Design 5 pages

1.4.5 Mechanical support

**Description of BaBar bars, bar boxes** We will reuse bar boxes from the Babar DIRC. Bar boxes will not be modified as it is considered too difficult to do. This has some disadvantages, for example, the old wedge, with its 6 mrad angle at the bottom surface, somewhat worsens the new camera optics by adding  $\sim 0.5$  mrad to the Cherenkov angle resolution. Another potential problem is that the glue has seen  $\sim 10$  years of radiation during the BaBar experiment. Extensive studies were performed with the BaBar dimuon data and no detrimental effect was found on the glue transmission [10]. However, we do need to be extra careful when transporting bar boxes, as it is not known if the Epotek 301-2 glue strength was not affected, and some tests will be required.

Figure 1.27 shows the BaBar DIRC bar box with its 12 Fused silica bars, each glued out of 4 bar segments 122 cm long [2]. Figure 1.28 shows the nominal dimensions of each bar including the wedge. In reality it is somewhat more complicated, as bar dimensions vary and each bar box is slightly different. This has been recorded in a form of spreadsheets [3]. Figure 1.29 shows

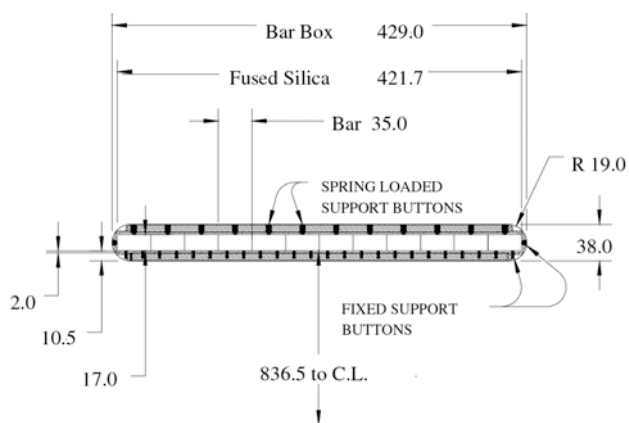


Figure 1.29: A cross-section of bar box with 12 bars [2].

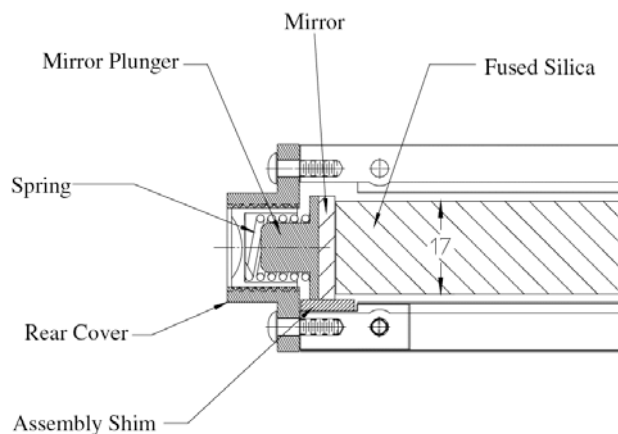


Figure 1.30: Bar end with a mirror [2].

a cross-section of bar box with 12 bars. Figure 1.30 shows the bar end with a mirror. There are altogether 12 bar boxes and 144 full-length bars in the entire system.

**Fused silica optics: New Wedge and FBLOCK** The New Wedge and the FBLOCK are made of radiation hard Fused silica Corning 7980. We visited the company and tested the material for stria. These could exist if the ingot is not thick enough and the FBLOCK would be part of the very bottom. Therefore manufacturing of FBLOCK requires somewhat thicker raw ingot and this issue should be remembered for the final production. The manufacturing was then split into three steps done in three different companies: (a) grinding final shapes about

1-2mm oversized, (b) polishing to final size and surface polish of better than 30A rms, (c) coating two FBLOCK's reflecting surfaces with aluminum with  $\text{SiO}_2$  overcoat to protect it, and (d) the final QC of finished pieces. Figures 1.31 show finished New Wedge and FBLOCK (before plating of two mirrors). These optical pieces were successfully produced, which demonstrates that the new camera optics is doable.

**FBLOCK mirror surfaces** It is absolute mandatory to have a very good surface cleanliness before the aluminum plating is attempted. Any contamination will result in peeling problems. FBLOCK's two aluminum plated mirror surfaces are protected by a  $\text{SiO}_2$  layer. Even though there is the protection layer, mirror surface are still fragile. Therefore front buttons do not act on the mirror surface directly. Instead we use small 1.25 inch dia., 1/16 inch thick quartz cookies as an interface between buttons and the mirror surface. The cookies are held to aluminized surface by Epotek 301-2 epoxy.

Another complicated issue is the FBLOCK shipping as it is very heavy and its polished surfaces and two mirrored sides can be easily damaged. Surfaces have to be protected by a plastic film during the shipment, but the film must not stick to mirror surface to cause peeling problems. Based on tests, we have decided to use Grafix plastic vinyl film in future, which adheres to surfaces via electrostatic forces, and it does not leave a surface pollution.

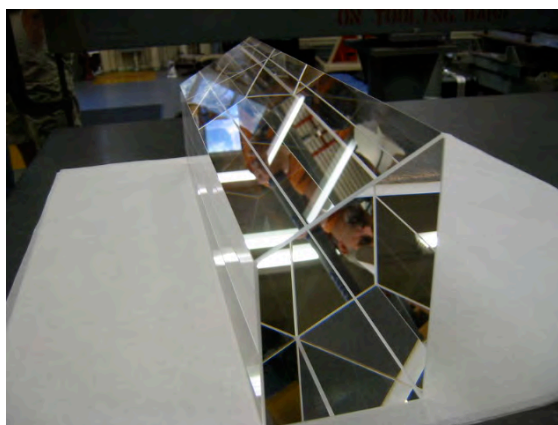
**Gluing Wedge to Bar Box Window** This optical coupling is done in the clean room. Figure 1.32 shows a detail of coupling of the New Wedge to the bar box. The coupling is done with the Epotek 301-2 optical epoxy of 25-50 micron thickness. The bottom of the New Wedge is aligned to the bottom of the bar. The New Wedge is centered left-right in the bar box window. This coupling is not possible to separate in future as we would risk damaging the bar box. Figure 1.24 shows the transmission of the Epotek-301-2 epoxy.

**Gluing FBLOCK to Bar Box Window** This optical coupling is done in situ, and is, in principle, removable. We set the gap between the





(a) FBLOCK after polishing but before plating.



(b) New Wedge after polishing.

Figure 1.31: New photon camera parts: New Wedge and FBLOCK.



(a) The bar box with the New Wedge in the clean room.



(b) Detailed view of the New Wedge and the bar box window.

Figure 1.32: Coupling of the New Wedge to the bar box.





Figure 1.35: Bar box storage at SLAC.

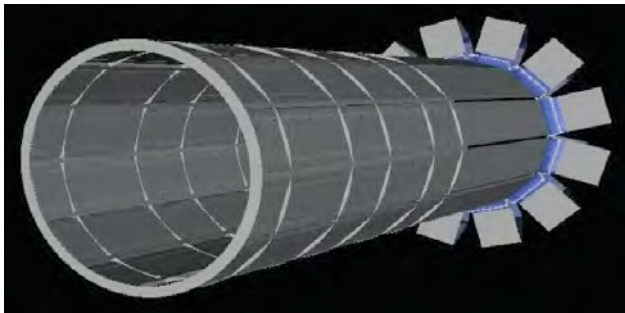


Figure 1.36: Overall view of the FDIRC layout with 12 bar boxes and 12 photon cameras.

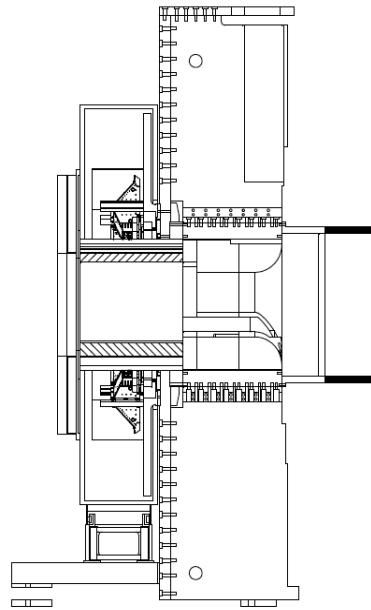
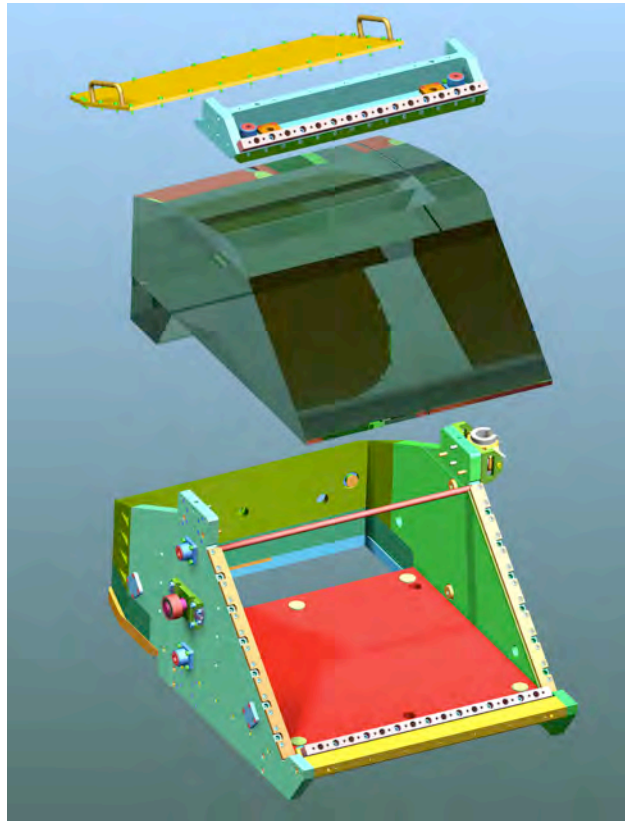
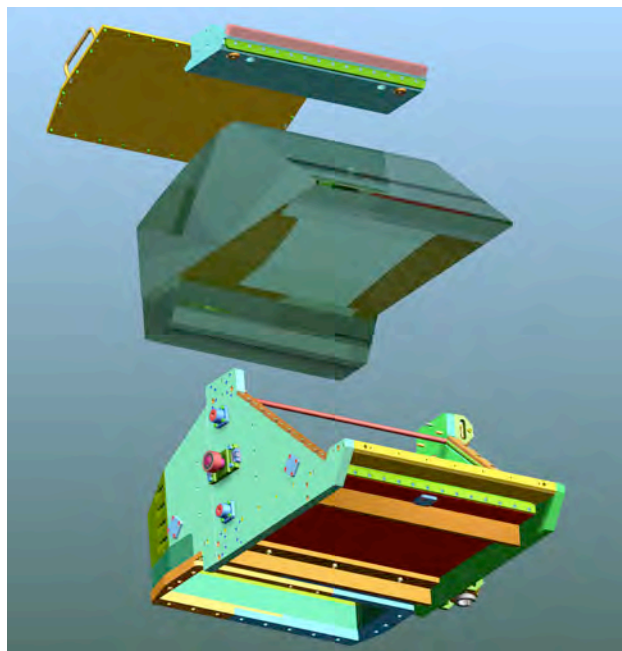


Figure 1.38: Side view of the FDIRC showing magnetic and background shields, and rails on which they move.

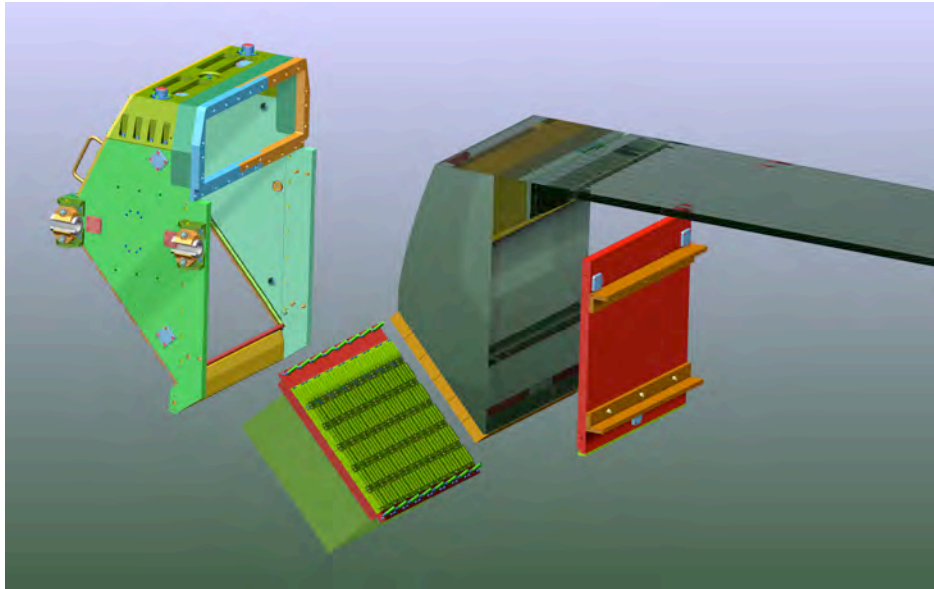


(a) Top view.

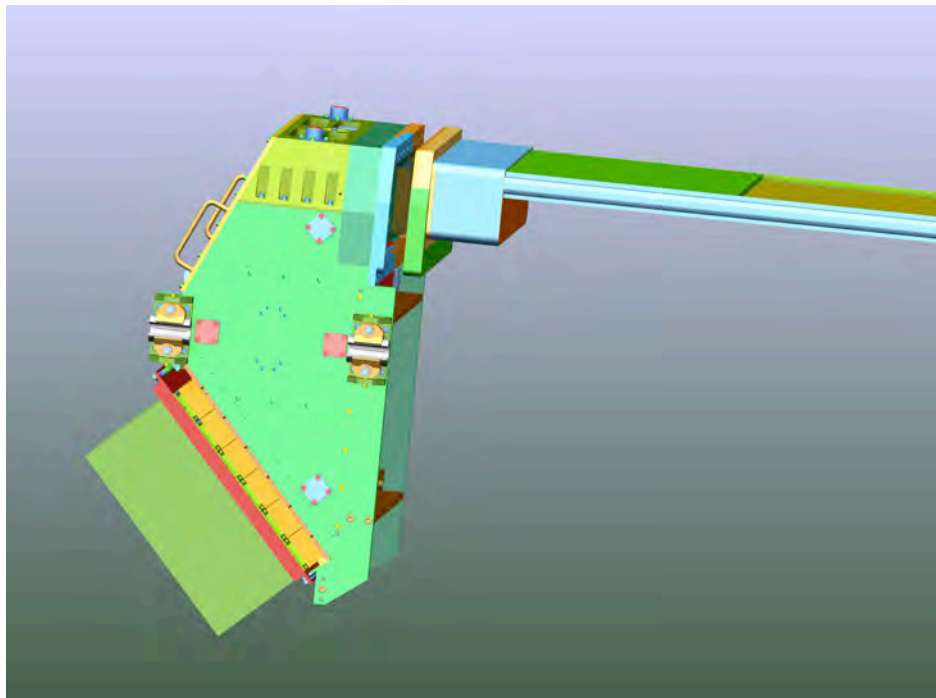


(b) Bottoms view.

Figure 1.33: Button support of FBLOCK optics in Fbox.

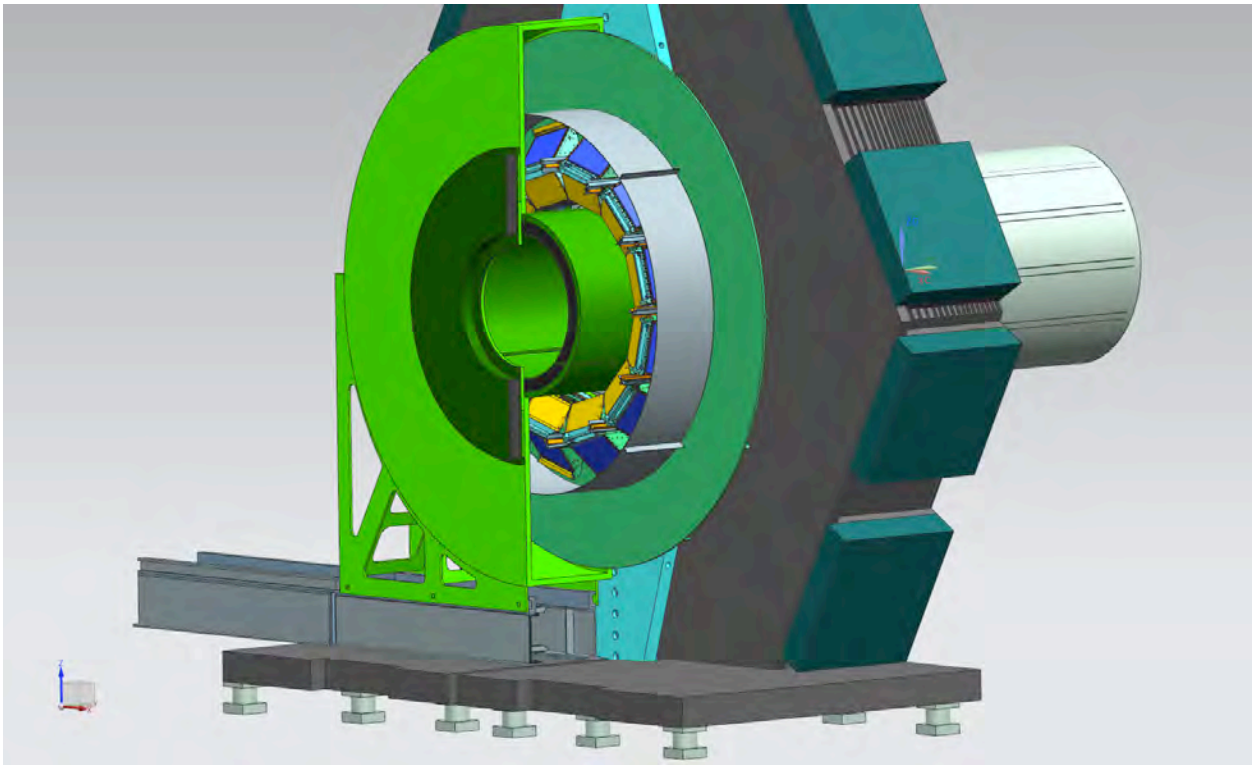


(a) Various components for the optics enclosure.

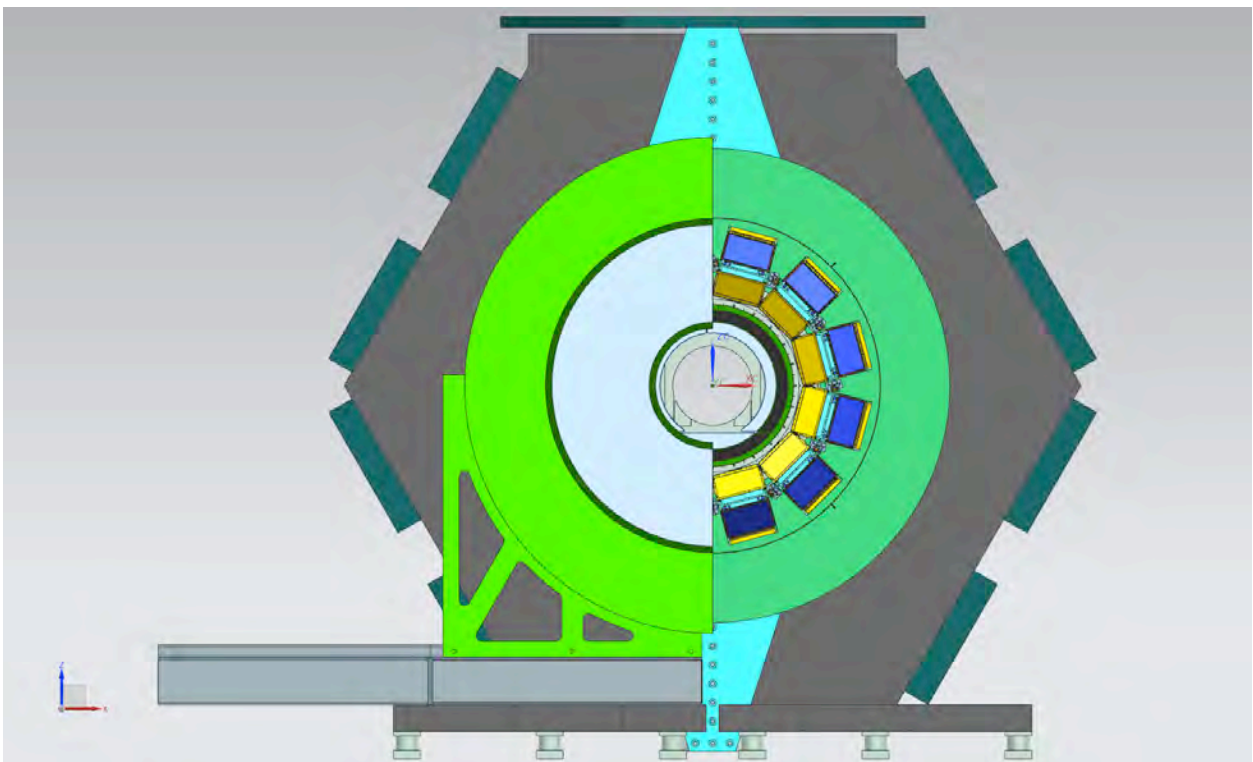


(b) Complete Fbox enclosure, including bar box.

Figure 1.34: Fbox enclosure of FBLOCK optics, including wedges, bars, detectors and electronics.



(a) A 3D view showing the new magnetic shield and background shields, and Fboxes.



(b) Front view showing 6 Fboxes, the rest is hidden behind magnetic and background shields.

Figure 1.37: FDIRC in the magnet.



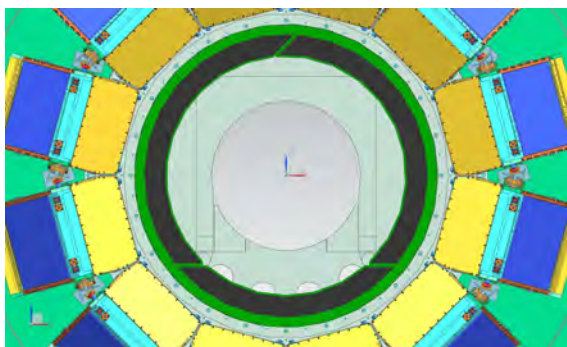


Figure 1.39: Detail view of Fboxes in the magnet.

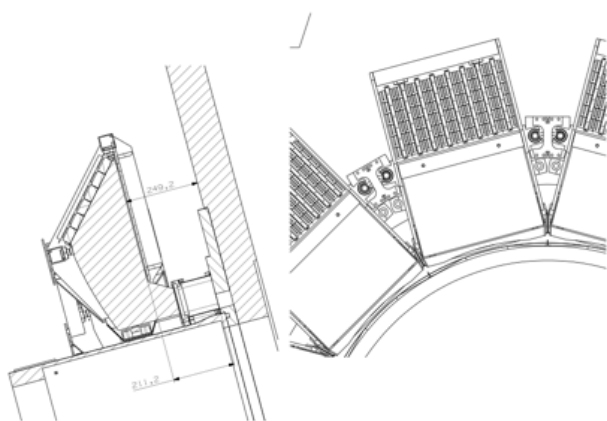


Figure 1.40: Fbox support in SuperB magnet.

new Wedge and the FBLOCK to 1mm, and fill it with Shin-Etsu 403 RTV. In case of some problem, one can separate two pieces by a razor wire, clean surface and could couple two surfaces again. Figure 1.24 shows the transmission of the Shin-Etsu 403 RTV.

**Fbox: Mechanical support of FBLOCK and Wedge** Figure 1.33 shows a detail of the photon camera. Plastic buttons prevent FBLOCK optical surfaces from touching of the Fbox's aluminum internal surfaces. Some buttons are fixed and some are spring loaded to take into account thermal effects. Placing the FBLOCK into the Fbox requires a very careful procedure as FBLOCK is very heavy ( $\sim 80\text{kg}$ ) and easy to be damaged. It was very useful to work out a step-by-step procedure [24] with a dummy plastic FBLOCK [25].

Figure 1.34 shows Fbox enclosure of the optics.

**Protection of optical surfaces** As one deals with internal reflections, all optical surfaces have to be very clean, and therefore every part of the Fbox was very carefully cleaned before a final assembly to prevent outgassing. In addition, optical surfaces are protected against the environmental pollution and the moisture condensation by flowing a boil-off  $\text{N}_2$  within the sealed Fbox. This required a very careful way to seal it with a combination of the DP-190 glue, Viton O-ring and the Gore gasket tape.

**Bar box storage at SLAC** Figure 1.35 shows present storage of 12 bar boxes taken away from BaBar. Bar boxes are supported on well pre-aligned shelves to prevent mechanical distortions. They are under a constant flow of the boil-off  $\text{N}_2$  and thermally insulated. The storage box is kept at a nominal temperature of  $18^\circ\text{C}$ . In addition, there is no light to prevent yellowing of the Epotek 301-2 glue.

**Support of Fbox in the SuperB magnet** Figure 1.36 shows the overall FDIRC detector schematic layout with 12 bar boxes, and 12 photon cameras. Figures 1.37 and 1.38 show overall mechanical view of the FDIRC in the SuperB experiment. Figures 1.39 and 1.40 show details of the Fbox support.

**Background shielding to protect electronics & detectors** We need background shielding to (a) reduce a contribution to the rate from FBLOCK part of FDIRC, which is located outside of the magnet, and (b) to reduce effect of radiation to detectors and electronics. Based on simulations, the dominant background in FDIRC is due to Radiative Bhabha scattering. The resulting background is mainly gammas, electrons, positrons and neutrons. The background estimate of the photoelectron rate, before this shield was installed into the MC simulation, was  $85\text{ kHz/double-pixel}$  coming from the active region of bar boxes within the magnet, and  $550\text{ kHz/double-pixel}$  coming from the FBLOCK section located outside the magnet. To reduce this rate, it is essential to provide

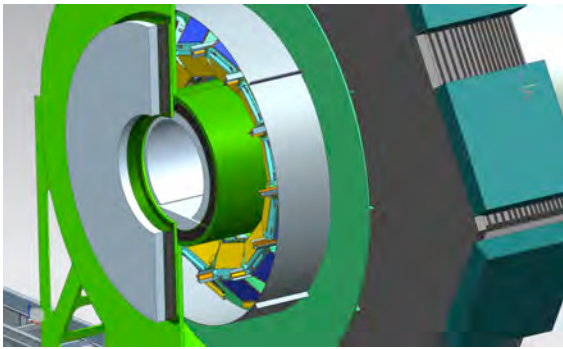


Figure 1.41: Details of local shielding around the FDIRC photon camera (a layer of 10 cm of Boron loaded polyethylene followed by 10-15 cm of lead-steel sandwich, located both on inner and front sides of the FBLOCK with its detectors and electronics).

a shield of the FBLOCK outside of the magnet. To design the shielding, one important constraint is an easy access to detectors and electronics, and second one is the overall weight of the shielding. Figure 1.41 shows the present concept of the FBLOCK shielding. It consists of 10 cm of Boron-loaded polyethylene layer sitting on 10-15 cm lead-steel sandwich, both located on inner radius and front side of the FBLOCK with its detectors and electronics. The front section of the shielding is moving on the magnetic door allowing a quick access to electronics and detectors - see Figure 1.41. After this shield was installed into the MC simulation, the FBLOCK contribution was reduced to ??? kHz/double-pixel and total dose of neutrons in the electronics region was reduced to ??? n/cm<sup>2</sup>/year.

**Bar box shipment to Italy** There are several issues to consider: (a) vibration and mechanical shocks, (b) thermal effects, (c) pressure changes, and (d) light exposure. Each bar box will have a container providing mechanical support and constant thermal environment. The vibrations and mechanical shocks will be solved by placing bar boxes on a precisely leveled support with a foam on top of it. The support structure will need telescopic mount to suppress large shocks. They will be thermally isolated and equipped

with active thermal blankets to keep temperature constant. We will also provide a  $N_2$  boil-off gas flow. Another important issue is pressure changes if the air transport will be used. The Hexel panels, used to construct bar boxes, do not have perforated walls, and therefore some stresses will be created. This has to be tested and carefully evaluated. Finally, bar boxes must not be left exposed to a strong light as one could yellow the Epotek 301-2 epoxy. (To be finished or changed after we conclude all discussions)

#### 1.4.6 Electronics readout, High and Low voltage

The electronics for the FDIRC can be seen as an upgrade of the electronics of the BABAR DIRC. The new requirements of the experiment (trigger rate, background, radiation environment) and FDIRC specific requirements (resolution, number of channels and topology) have led to a similar but new design of the electronics chain.

The FDIRC electronics will handle 18,432 channels per each of 12 sectors. The electronics chain is based on a high resolution and high count rate TDC, a time associated charge measurement with 12 bit resolution, and an event data packing, sending data frames to the data acquisition system (DAQ). The target timing performance of the overall electronics chain is a time resolution of 100 ps rms. It has to deal with hit rate of 100 kHz per channel, a trigger rate up to 150 kHz, and a minimum spacing between triggers of about 50 ns.

The radiation level is expected to be less than 100 rads per year. The use of radiation tolerant components or off-the-shelf radiation-qualified components is mandatory. However, the expected energy of the particles may make the latch-up effect almost impossible. Thus the design has to take into account only Single-Event-Upsets. We selected the Actel family FPGA components for their non-volatile flash technology configuration memories, which are well adapted to radiation environment.

Several architectures have been considered: (a) all electronics directly mounted on the FBLOCK, (b) all electronics mounted next to the detector and linked to PMTs by cables, and

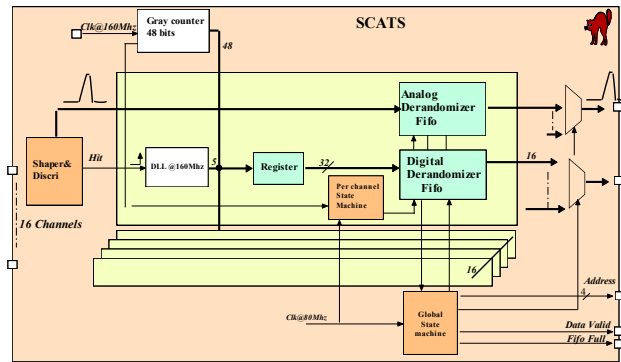


Figure 1.42: SuperB FDIRC TDC chip (SCATS) block diagram.

(c) a part of it on the detector (the Front-end boards) and the other part, called crate concentrator, situated close to the detector (this board is in charge of interfacing with the Front-end, reading out event data, packing and sending it to the DAQ).

The first solution has been chosen as baseline for the TDR for 2 main reasons: (a) The cost of cables (PMT to Front-end boards) is estimated to be close to 200 kEuros (1/3 of the price of the overall electronics cost), making this solution too expensive. Moreover, the possible option to have pre-amps on the PMT bases doesn't prevent from having electronics and power supplies on the detector. (b) The large amount of data per channel leads to have the L0 derandomizer and buffer on the Front-end boards. The FCTS receiver could be individually located on each Front end board but the number of cables needed pushes to distribute all the control signals on a backplane. Consequently the board dedicated to receiving and transmitting FCTS signals on the backplane naturally tends to also become the event data concentrator and the link to the DAQ. The baseline design assumes a 16-channel TDC ASIC, offering the required precision of 70 ps rms, embedding an analog pipeline in order to provide an amplitude measurement transmitted with the hit time. Thanks to a 12-bit ADC, the charge measurement will be used for electronics calibration, monitoring and survey purposes. The Front-end board FPGA synchronizes the process, as-

sociates the time and charge information and finally packs them into a data frame which is sent via the backplane to the FBLOCK control board (FBC). The FBC is in charge of distributing signals coming from the FCTS and ECS, packing the data received from the FE boards to a n-event frame including control bits and transferring it to the DAQ.

**FDIRC electronics (Amp/TDC/ADC)** An earlier version of TDC chip, offering a similar resolution, has already been designed for the SuperNemo experiment. It provides a time measurement with both a high resolution (70 ps RMS) and a large dynamic range (53 bits). The architecture of this chip is based on the association of Delay Locked Loops (DLLs) with a digital counter, all of these components being synchronized to a 160 MHz external clock.

The SuperB chip, SCATS, will keep the same philosophy but the high input rate requirement lead to a complete re-design of the readout part, in order to minimize the dead time per channel by increasing the data output speed. Instead of registers and multiplexer, which are the bottlenecks of the SuperNemo chip readout, it makes use of an individual FIFO memory per channel in order to derandomize the high frequency bursts of input data. With this architecture, data from the DLLs and the coarse counters are transferred into the FIFO memory within two clock cycles. When the transfer is complete, the channel is automatically reset and ready for the next hit. Simulations of the readout state machine showed an output FIFO data rate capability of 80 MHz. Time ranges for the DLLs and the coarse counter can be easily customized by adjusting the output data format (16, 32, 48 or 64 bits). Therefore, the chip is suitable for various applications with either high count rate and short integration time or low count rate and long integration time. Figure 1.42 shows the block diagram of SuperB FDIRC TDC chip (SCATS).

A FIFO depth of 8 words has been selected after simulation with an exponential distribution model of delta time between hits (mean rate 1MHz) applied to inputs. To design this FIFO

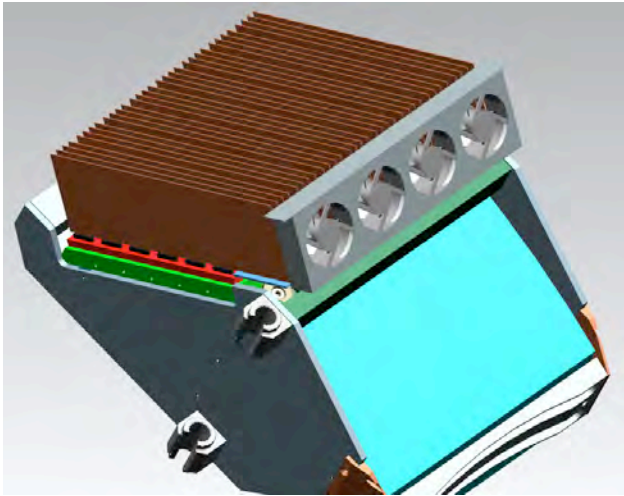


Figure 1.43: FBLOCK equipped with electronics and its cooling.

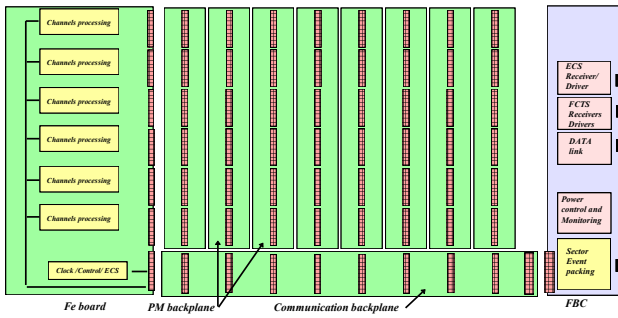


Figure 1.44: Front-end crate: PMT backplane, Communication backplane, FE-board, FBLOCK controller (FBC).

a full custom RAM has been developed. It permits reducing the size of the chip and consequently its cost. The chip is designed using known and proved mitigation techniques to face single event upset (SEU) issues due to the low-level radiation environment. The first version of the chip without the analog FIFO and the discriminator has been submitted in November 2011. We plan to submit by mid 2012 one chip dedicated to the currently missing parts: (a) A low walk discriminator receiving the PM outputs and sending logic signal to the TDC part of the chip, and (b) an analog pipeline synchronized with the digital FIFO and providing analog output for charge measurement. After

testing and validation, a final version of SCATS will then be assembled and submitted end 2013. The Front-end Crate: The board input will fit the topological distribution of the PM on the FBLOCK. The PMTs are arranged as a matrix of 6 in vertical direction by 8 in horizontal direction. Each column of 6 PMTs will fit to one FE board. One vertical backplane (PMT Backplane) will interface between the 4 connectors of each PM base to one connector of FE board - see Fig. 1.44. The PMT backplane is also in charge of distributing the High Voltage, thus avoiding HV cables to pass over the electronics. The FB crate will use as much as possible the elements of a commercial crate, in order to avoid the design of too many specific elements like board guides. Figure 1.43 shows the FBLOCK with the front-end electronics.

The Communication Backplane: Distributes the ECS and FCTS signals from the FBC to the 8 FE boards thanks to point to point LVDS links. Connects each FE board to the FBC for data transfer. A serial protocol will be used between FE board and the FBC in order to reduce the number of wires and consequently ameliorate the reliability.

Then PMT Backplane: Interface the 6 PMTs of a column to one FE board. The 32 channels of each PM distributed on the 4 connectors of the PM base are merged into one connector to

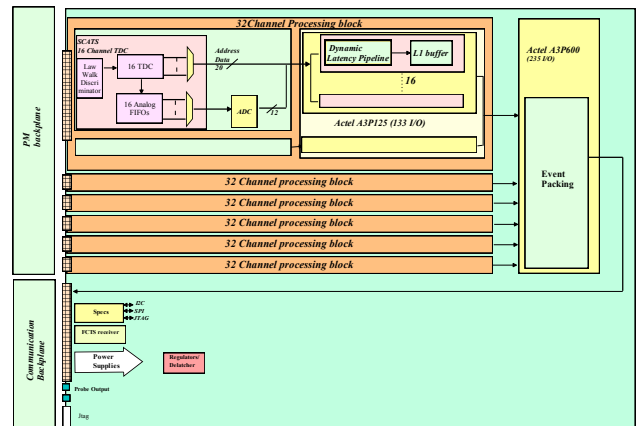


Figure 1.45: Front-end board connected to the backplanes.



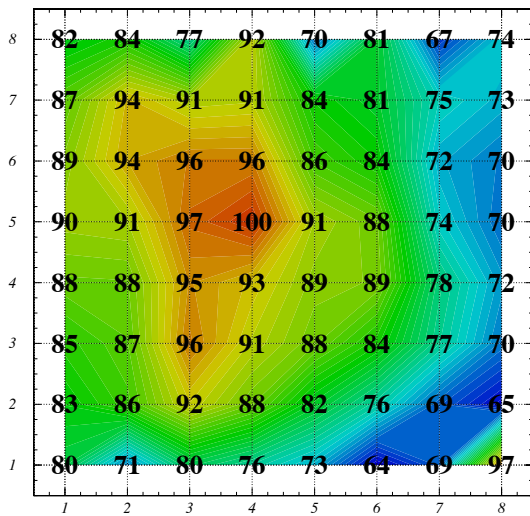


Figure 1.46: A relative pulse height response of H-8500 anodes to a pulse coupled to the last dynode [26].

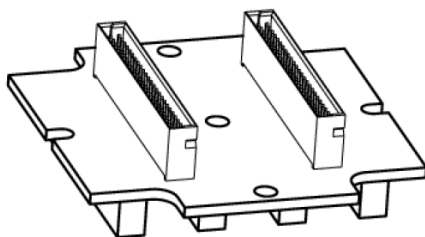


Figure 1.47: A single motherboard for each H-8500.

get into the Front end connector. It also insures the ground continuity between FE board crate FBLOCK. Taking into account the isolation constraints between plans of the printed circuit board, it distributes the High Voltage to the PM base.

**Cooling and Power Supply:** The electronics is located on the detector in a place enclosed by the doors. There are 2 major consequences: one is the problem of the cooling which must be carefully studied in terms of reliability and capability, and the second is that the location is naturally shielded against magnetic field. Consequently the use of magnetic

sensitive components as coils or fan trays is possible. An estimate of the overall electronics consumption lead to  $\sim 6.1$  kW, not including the external power supplies. This can be broken down to individual contributions as follows: (a) electronics: 0.325 W/channel, 500 W/sector, and 6 kW/system; (b) HV resistor chain: 0.19 W/tube, 9.1 W/sector, and 109 W/system. The cooling system must be designed in order to maintain the electronics located inside at a constant temperature close to the optimum of 30 degrees. The air inside the volume must be extracted while the dry, clean temperature controlled air will be flowing inside. Each FB crate will have its own fan tray like in a commercial crate. Targeting a difference of 10 degrees between inside and outside temperature drives to a rough estimate value of 300 m<sup>3</sup> per hour per crate. 4000 m<sup>3</sup> per hour can be considered as the baseline value for the whole detector.

**The Front-end Board:** One Front-end board (FE-board) is made of 6 channel-processing blocks handling 192 channels of one column of PMTs. Each channel-processing block has 2 SCATS chips, 2 ADCs, and one Actel FPGA and some synchronizing logic. The FPGA controls both TDC and ADC. Upon a reception of the L1 trigger, it associates time and charge for the event and packs the data into an event frame. The FE-board transfers the event frame in differential LVDS to the FBC via the communication backplane. Figure 1.45 shows the architecture of the FE-board connected to the backplanes

**Electronics calibration** H-8500 PMT has a AC connection the the last dynode, and this can be used either for triggering or calibration purposes. One can do the calibration with HV off by injecting a pulse and looking at response of all anodes. Figure 1.46 shows a relative pulse height response of 64 anodes to such pulse injection [26]. It is not uniform, but it could be useful to identify possible electronics problems.

**Motherboard** Figure 1.47 shows the present concept of one single motherboard. Row of 6 such motherboards will be pre-aligned with a

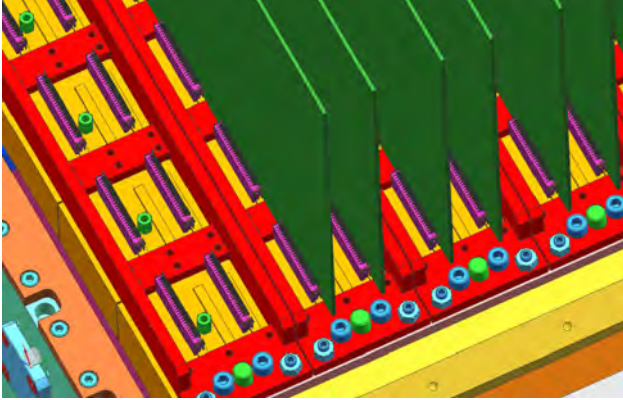


Figure 1.48: FDIRC electronics on one FBLOCK (detectors and motherboard are in yellow, electronics boards are in green).

fixture, so one can safely plug in a single electronics board - see Fig. 1.48. There will be 16 electronics boards per one single FBLOCK. The electronics board will either inserted or extracted with a help of tools and rails, a similar procedure as in some commercial crates (rails are not shown on Fig. 1.48).

Figure 1.49 the complete photon camera with the electronics for 48 H-8500 PMTs and 1536 double-pixels.

#### Support services [Christophe](#)

**HV distribution and HV power supplies** Resistor chain of each tube draws  $\sim 150\mu\text{A}$  at  $-1.0$  kV. We are planning to gang together 6 tubes for one HV channel. The easiest and neatest way to arrange tube ganging is via a HV harness that corresponds to one motherboard column, and one HV channel. Therefore, each HV power supply channel should be able to provide a max current capacity of 1.5-2 mA to be able to serve 6 tubes.

If one tube fails, for example, and draws a large current, we would be forced to shut down 6 tubes temporarily until an access can be arranged and one HV connector is removed from that particular dead tube. Such tube would have to be recognized from data monitoring. During the access, one will remove the connector from the dead tube, place on it a protec-

tive plastic termination to avoid an accidental sparking, and continue running with one dead tube until it would be replaced during a longer shutdown.

The HV power supply will be CAEN, Model V6533, or equivalent. It has 6 independent channels per module, each channel capable of providing up to 4kV and 3mA. The entire FDIRC system would need 16 such HV power supplies, i.e., altogether 96 independent HV channels. They will be located behind the background shield in the non-radiation area. There will be 96 long HV cables going to the harness distribution boxes.

#### 1.4.7 Integration issues [2 pages](#)

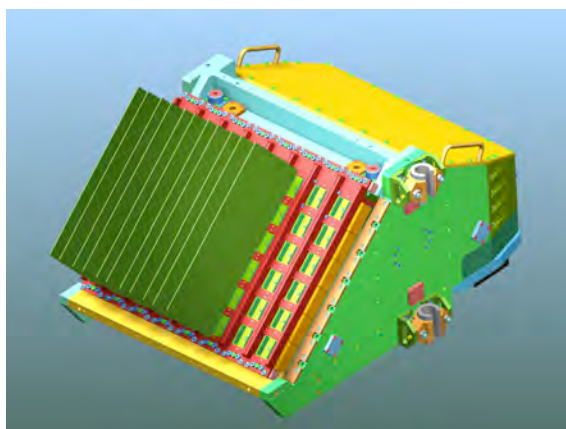
**Background shield and access to detector maintenance** Because the front part of the FBLOCK background shield is mounted on the magnetic door, which is on rails, it will be easy to move it sideways to allow a quick access to the detectors and electronics - see Figure 1.41.

#### Earthquake analysis of FBLOCK & bar box structure [Benettoni, Simi](#)

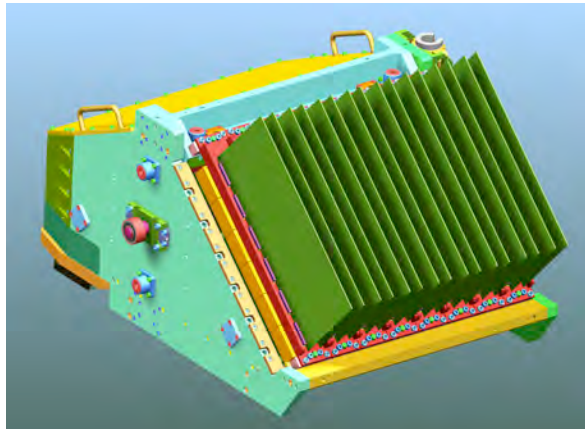
**PMT protection (helium, large backgrounds)** It is well known that the PMT operation can be affected by a helium contamination, which can penetrate the PMT glass. These atoms convert to ions in the avalanche process, which can drift back to the photocathode creating secondary photoelectrons, often called after pulses. Therefore, just like in case of the BaBar DIRC, which had  $\sim 11,000$  PMTs, we assume that any helium leak checking close to the SuperB detector by accelerator people must not be allowed. Even if it is done far away in the tunnel, air draft could bring it to the detector. We will need a helium detector to monitor this.

Reference [27] summarizes the the effect of helium contamination on a PMT. We should stress, however, that we did not do any experimental study with the H-8500 tube up to this point, i.e., we assume that it behaves the same way as any other PMT from this point of view, i.e., that its 64 feedthroughs do not affect it.

The ion contamination in a PMT can be measured by measuring the after pulsing rate. Fig-



(a) Photon camera with its electronics.



(b) Photon camera with its electronics.

Figure 1.49: Photon camera with a high density electronics for 48 H-8500 PMTs.



Figure 1.50: A time spectrum of after pulses showing  $H^+$ ,  $H_2^+$  and  $He^+$  contamination [26].

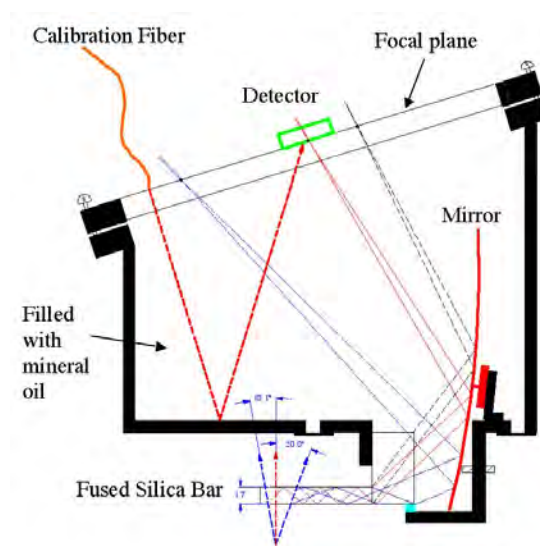


Figure 1.51: The 1-st FDIRC single-bar prototype employing a spherical mirror, oil-filled photon camera, and highly-pixelated photon detectors [8], [9], [11].

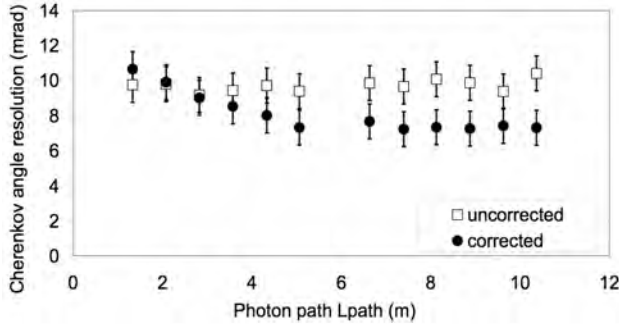


Figure 1.52: Measured Cherenkov angle resolution using all pixels (a) without the chromatic correction, (b) with the chromatic correction where the chromatic error is corrected by timing, and plotted as a function of photon path in the bar [11].

Figure 1.50 shows how the  $H^+$ ,  $H_2^+$  and  $He^+$  ion contamination [26] affects a time spectrum of afterpulses in the H-8500 tube. The total measured rate of after pulses was less than  $\sim 1\%$  rate for this tube. This measurement will have to be part of PMT QC procedure to weed out bad tubes. It will be useful to repeat it periodically on some tubes during the SuperB experiment.

The H-8500 PMT sensitivity to large background were discussed in chapter discussing the PMT rate and aging issues. Here we add only that a PMT protection strategy, for example an automatic HV lowering to 80% value if a certain background level is reached, has yet to be developed.

#### 1.4.8 DAQ and computing 1 page

Data flow [Breton](#)

Feature extraction in the ROM [Breton](#)

#### 1.4.9 FDIRC R&D Results until now 2-3 pages

**Test beam results from the 1-st FDIRC prototype** Figure 1.51 shows the prototype. This prototype was tested in the 10 GeV electron test beam at SLAC. This beam entered the bar perpendicularly. It was very successful R&D program resulting in a number of very useful re-

sults [8], [9], [11], which can be summarized as follows:

- Learned how to operate new fast highly pixilated detectors (Hamamatsu H-8500 and H-9500 MaPMTs, and Burle MCP-PMTs). The H-9500 MaPMT was arranged to have 3 mm x 12 mm pixel size, other two tubes had 6 mm x 6 mm pixels.
- Test achieved  $\sim 10x$  better single-electron timing resolution than DIRC:  $\sigma_{H-8500} \sim 240$  ps,  $\sigma_{H-9500} \sim 235$  ps, and  $\sigma_{MCP-PMT} \sim 170$  ps.
- Learned how to design a new optics, which is a combination of pin hole coupled to focusing optics, resulting in  $\sim 25x$  smaller photon camera than the BaBar DIRC SOB.
- This was the very first RICH detector establishing that the chromatic error can be corrected by timing - see Fig. 1.52. To be able to do such correction, one needs to achieve a timing resolution at a level of  $\sim 200$  ps per single photon, and the photon path length needs to be longer than 2-3 meters. The fact that FDIRC bars are longer due to a penetration of the magnet iron helps to improve this correction.
- With 6 mm size pixels we could reproduce BaBar DIRC performance of Cherenkov angle resolution of  $\sim 10$  mrad per single photon if we do not perform the chromatic correction. With the chromatic correction one could improve this resolution by 0.5-1 mrad for photon path lengths longer than 2-3 meters - see Fig. 1.52.
- With 3 mm size pixels we could substantially improve on the FDIRC performance - see Figure 1.53. Figure 1.54 shows the expected overall PID performance relative to the BaBar DIRC. Clearly, smaller binning in the y-direction would be beneficial to improve the overall performance. However, Hamamatsu has strongly discouraged us to switch to the H-9500 tube as it could



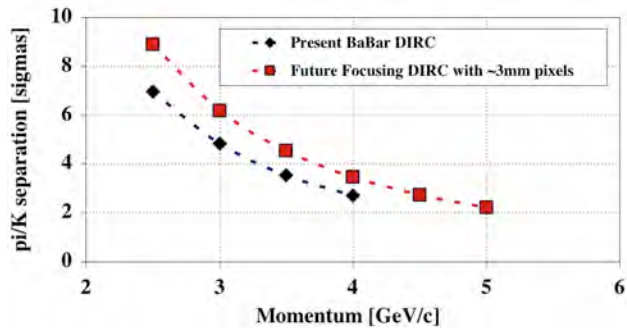


Figure 1.54: Expected  $K - \pi$  separation as a function of momentum for an FDIRC detector equipped with H-9500 MaPMTs with 3 mm x 12 mm pixels, compared to the BaBar DIRC performance [11].

not guarantee the deliveries. In addition, the cost of H-9500 tube would be higher.

- Discovered a new Cherenkov ring aberration, which worsens the resolution near the Cherenkov wings - see Figures 1.6, 1.7.

**CRT test results from the 1-st FDIRC prototype** The first prototype was also tested in the cosmic ray telescope (CRT) [22]. The SLAC CRT setup consists of energy absorber made of 4 ft-thick iron, which provides a muon energy cut-off of 1.6 GeV. It also provides tracking with 1.5 mrad resolution over angular range of dip angles within 15 degrees. This was also a significant test because it allowed to investigate the Cherenkov angle resolution with 3D tracks [28]. Results can be summarized as follows:

- We learned how to handle 3D tracks in the Cherenkov angle analysis (during the beam test tracks entered perpendicularly [8], [9], [11]).
- Tail in the Cherenkov angle distribution is related to the ambiguity treatment and it is more significant for 3D tracks. The 1-st FDIRC prototype had only two ambiguities: we could not tell a sign of photon vector in the x-direction for photons exiting

the bar end, and therefore in the analysis we had to consider both signs. In the final FDIRC prototype we will have 6 ambiguities. This ambiguity effect enhances the tail as one cannot always reject wrong solution, and it is magnified by a presence of background such as delta-rays or showers accompanying CRT muons. The CRT setup is very good to test to learn how to deal with it. The major conclusion is that one has to use a quantity  $dTOP = TOP_{measured} - TOP_{expected}$ , where  $TOP =$  time-of-propagation of photon in the bar. One makes a tight cut on  $dTOP$  and this helps to reject the background, however, it does not help the ambiguity problem.

- Running CRT continuously allowed to test various versions of electronics very conveniently, and under a real conditions producing the Cherenkov angle resolution. So far, every electronics used in the CRT setup, was caught to have some problems, which then had to be fixed. Therefore, we consider the CRT test to be very useful. It is interesting to point out that Belle-II TOP people are trying to create a similar CRT setup.
- The CRT trigger was also used to trigger PiLas laser diode, which provided a single photoelectron monitoring of all pixels all the time while we were running. The laser trigger did not overlap the CRT data to avoid a confusion. This task allowed to study a stability of FDIRC timing.
- This feature has not been done in studies so far, but we plan to test the Final FDIRC prototype at high rate background in the CRT setup. This will be done by admixing an asynchronous random light source to the laser calibration signal, while taking a normal CRT data. This task will be accomplished with a fiber mixer, which will mix the laser signal with the random light source. In this way we can study the reconstructed Cherenkov resolution as a function of the random background in a controlled

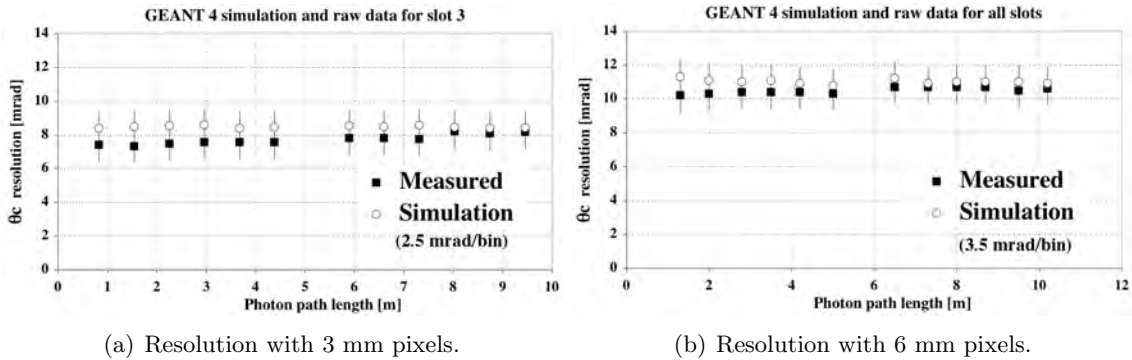


Figure 1.53: Measured and simulated Cherenkov angle resolution without chromatic correction [11]

way, and see at what point the reconstruction algorithm breaks down. At the same time we will be monitoring the timing resolution deterioration using the laser signal.

**Scanning setups to test H-8500 PMTs and Electronics** We have several PMT scanning setups located at SLAC, Maryland, Bari, Padova and Orsay. These setups differ in their capabilities, designs and electronics. Although these setups did not use yet the final electronics, nevertheless, they were very useful to reveal many H-8500 detector details. So far, these topics were studied in some detail: (a) efficiency uniformity across PMT for 15 tubes, (b) gain uniformity for 15 tubes, (c) cross-talk, (d) charge charing, (e) after-pulses, (f) pre-pulses (amplification starts on 1-st dynode), (g) anode response to pulses on the last dynode (for calibration purposes), etc. We used many results from these tests throughout this TDR document.

**1.4.10 Ongoing FDIRC R&D 1-2 pages**

**Experience with the final FDIRC prototype in CRT Vavra, Padova, Bari**

**1.4.11 System Responsibilities and Management 1-2 pages**

**Management structure SLAC, LAL, Padova, Bari**

**Institutional breakdown by task SLAC, LAL, Padova, Bari** Table 1.2 shows a breakdown of tasks by institutions. This is only an example at the moment. It has to be agreed by everybody.

**1.4.12 Cost, Schedule and Funding Profile 1-2 pages**

**Budget Vavra, Arnaud, Mazziotta, Simi** Table 1.3 shows a breakdown of costs. The cost of FDIRC optics is based on our experience building the FDIRC prototype and it is judged fairly real. It is interesting to point out that the cost came down by a factor two by the time we finished building it, mainly because we were working directly with companies involved building it. Therefore we have real companies behind each task, and, in principle, we are ready to build it. But one should realize that this is the cost as of the end of 2011.

**Schedule and Milestones Vavra, Arnaud, Mazziotta, Simi**

Critical path items	Vavra, Arnaud, Mazziotta, Simi
=====	=====

Item	Task	Institution
1	FBLOCK optics	SLAC, Padova, Bari
2	Wedge optics	SLAC, Padova, Bari
3	Gluing Wedge to bar box	SLAC
4	Fbox	Padova, Bari, SLAC
5	Assembly of optics to Fbox	SLAC, Padova, Bari
6	Fbox mechanical support	Padova, Bari, SLAC
7	Electronics	LAL
8	Motherboard	Padova, LAL, Bari
9	Electronics cooling	LAL, Padova
10	Detector procurement	???
11	Detector testing	Maryland, LAL, Bari, Padova, SLAC
12	Final FDIRC testing in CRT	SLAC, Maryland, LAL, Bari, Padova
13	High voltage	Padova, ???
14	Low voltage	LAL, ???
15	Fiber calibration	???
16	Fast simulation	LAL, ???
17	Full simulation	Maryland, ???
18	Final installation in SuperB	SLAC, Padova, Bari
19	Thermal protection	LAL, Padova
20	Background monitoring	SLAC, LAL, Padova, ???
21	Helium protection	Bari, ???
22	Boil-off nitrogen distribution	???
23	Essential services	???
24	On-line monitoring	???

Table 1.2: Institutional breakdown by task.

Item	Task	Cost
1	FBLOCK + Wedge, material & raw finish, 12 + 2 pieces	\$58.9k ea., \$824.6k total
2	Wedge, polishing only, 12 + 2 pieces	\$1.5k ea., \$21k total
3	FBLOCK, polishing only, 12 + 2 pieces	\$18k ea., \$252k total
4	FBLOCK, mirror plating, 12 + 2 pieces	\$28k total
5	FBLOCK, Wedge and Fbox cleaning and QC, 12 + 2 pieces	\$50k total
6	Gluing Wedge to bar box, 12 pieces	\$15k total
7	Fbox material and construction	???
8	Optics assembly into Fbox mechanical structure	???
9	Optics shipping with full value insurance within US	\$84k total
10	Fbox shipping to Italy and full value insurance	???
11	Bar box shipping to Italy and full value insurance	???
12	Fbox mechanical support	???
13	Electronics	???
14	Motherboard	???
15	Electronics cooling	???
16	Detector, 650 H-8500D tubes, selected for QE 24% min	\$2.8k ea., \$1.82M total
17	Detector testing	???
18	High voltage	???
19	Low voltage	???
20	Fiber calibration	???
21	Final installation in SuperB	???
22	Background monitoring	???
23	Helium protection	???
24	Boil-off nitrogen distribution	???
25	Essential services	???

Table 1.3: Cost breakdown by task.



# Bibliography

- [1] B. Ratcliff, SLAC-PUB-5946, 1992; and *Simple considerations for the SOB redesign for SuperB*, <http://agenda.infn.it/conferenceDisplay.py?confId=458>, SuperB PID meeting, March 18, 2008.
- [2] I. Adam *et al.*, Nucl. Instrum. Methods Phys. Res., Sect. A **583**, 281 (2007).
- [3] J. Va'vra, spreadsheet accompanying each bar box construction, 1999.
- [4] J. Va'vra *et al.*, Nucl. Instrum. Methods Phys. Res., Sect. A **639**, 404 (2011)282-286.
- [5] J. Va'vra, SuperB workshop, Perugia, June 2009, <http://agenda.infn.it/conferenceDisplay.py?confId=1161>, and SuperB workshop, October 2009, SLAC, <http://agenda.infn.it/conferenceDisplay.py?confId=1742>.
- [6] J. Va'vra *et al.*, Nucl. Instrum. Methods Phys. Res., Sect. A **606**, 404 (2009)404-410.
- [7] E. Kravchenko, SuperB workshop, June 2009, Perugia, <http://agenda.infn.it/conferenceDisplay.py?confId=1161>.
- [8] J. Benitez *et al.*, SLAC-PUB-12236, October 2006.
- [9] J. Va'vra *et al.*, SLAC-PUB-12803, March 2007.
- [10] N. Arnaud, Study of the glue transmission with di-muon BaBar data, 2009.
- [11] J. Benitez *et al.*, Status of the Fast Focusing DIRC (FDIRC), Nucl. Instrum. Methods Phys. Res., Sect. A **595**, 104 (2008) 104-107.
- [12] J. Va'vra, *Simulation of the FDIRC optics with Mathematica*, SLAC-PUB-13464, 2008; and *Focusing DIRC design for SuperB*, SLAC-PUB-13763, 2009.
- [13] D. Roberts, SuperB workshop, October 2009, SLAC, *Geant4 model of FDIRC*, <http://agenda.infn.it/conferenceDisplay.py?confId=1742>.
- [14] C. Field *et al.*, *Development of Photon Detectors for a Focusing DIRC*, Nucl. Instrum. Methods Phys. Res., Sect. A **553**, 96 (2005) and SLAC-PUB-11107, 2004.
- [15] D. Breton, E. Delagnes and J. Maalmi, *Picosecond time measurement using ultra fast analog memories*, talk and proceedings at TWEPP-09, Paris, September 2009.
- [16] C. Beigbeder, Status of FDIRC electronics, SuperB workshop, Elba, May 2011, <http://agenda.infn.it/conferenceOtherViews.py?view=standard&confId=3352>.
- [17] G. Varner, Nucl. Instrum. Methods Phys. Res., Sect. A **538**, 447 (2005), Nucl. Instr. Methods Phys. Res., Sect. A **538** (2005) 447.
- [18] G. Varner, Deeper Sampling CMOS Transient Waveform Recording ASICs, TIPP conference, June, 2011, Chicago, [http://www.phys.hawaii.edu/~varner/TIPP\\_DeepWFS\\_ASICs\\_10jun2011\\_varner.pdf](http://www.phys.hawaii.edu/~varner/TIPP_DeepWFS_ASICs_10jun2011_varner.pdf).
- [19] J. Va'vra, FDIRC status, SuperB workshop, Elba, May 2011, <http://agenda.infn.it/conferenceOtherViews.py?view=standard&confId=3352>.

- [20] C. Pauly, Single photon detection with H-8500 MaPMTs for the CBM RICH detector, , DPG Munster, March 2011, <http://www.gsi.de/documents/DOC-2011-Mar-233-1.pdf>.
- [21] P. Abbon *et al.*, Nucl. Instrum. Methods Phys. Res., Sect. A **595**, 204 (2008).
- [22] J. Va'vra, *SLAC cosmic ray telescope facility*, SLAC-PUB-13873, Jan. 2010.
- [23] J. Va'vra, FDIRC status, SuperB workshop, London, September 2011, <http://agenda.infn.it/conferenceOtherViews.py?view=standard&confId=3827>.
- [24] M. Benettoni, Fbox assembly procedure, SuperB workshop, Elba, May 2011, <http://agenda.infn.it/conferenceOtherViews.py?view=standard&confId=3352>.
- [25] N. Mazziota, Activity in Bari, SuperB workshop, London, September 2011, <http://agenda.infn.it/conferenceOtherViews.py?view=standard&confId=3827>.
- [26] G. Simi, H-8500 studies, SuperB workshop, Frascati, December 2011, <http://agenda.infn.it/conferenceOtherViews.py?view=standard&confId=4107>.
- [27] N. Mazziotta, A study of afterpulse effect due to Helium permeation in the H8500 MaPMT, SuperB workshop, Frascati, December 2011, <http://agenda.infn.it/conferenceOtherViews.py?view=standard&confId=4107>.
- [28] K. Nishimura *et al.*, *A detailed study of FDIRC prototype with waveform digitizing electronics in cosmic ray telescope using 3D tracks*, to be published.